The Astrophysical Journal, 684:1–17, 2008 September 1

HOW VERY MASSIVE METAL-FREE STARS START COSMOLOGICAL REIONIZATION

John H. Wise[1,2] and Tom Abel[1]

Received 2007 October 12; accepted 2008 May 10

ABSTRACT

The initial conditions and relevant physics for the formation of the earliest galaxies are well specified in the concordance cosmology. Using ab initio cosmological Eulerian adaptive mesh refinement radiation hydrodynamical calculations, we discuss how very massive stars start the process of cosmological reionization. The models include nonequilibrium primordial gas chemistry and cooling processes and accurate radiation transport in the case B approximation using adaptively ray-traced photon packages, retaining the time derivative in the transport equation. Supernova feedback is modeled by thermal explosions triggered at parsec scales. All calculations resolve the local Jeans length by at least 16 grid cells at all times and as such cover a spatial dynamic range of $\sim 10^6$. These first sources of reionization are highly intermittent and anisotropic and first photoionize the small-scale voids surrounding the halos they form in, rather than the dense filaments they are embedded in. As the merging objects form larger, dwarf-sized galaxies, the escape fraction of UV radiation decreases and the H II regions only break out on some sides of the galaxies, making them even more anisotropic. In three cases, SN blast waves induce star formation in overdense regions that were formed earlier from ionization front instabilities. These stars form tens of parsecs away from the center of their parent DM halo. Approximately five ionizing photons are needed per sustained ionization when star formation in $10^6\ M_\odot$ halos is dominant in the calculation. As the halos become larger than $\sim 10^7\ M_\odot$, the ionizing photon escape fraction decreases, which in turn increases the number of photons per ionization to 15–50, in calculations with stellar feedback only. Radiative feedback decreases clumping factors by 25% when compared to simulations without star formation and increases the average temperature of ionized gas to values between 3000 and 10,000 K.

Subject headings: cosmology: theory — galaxies: formation — intergalactic medium — stars: formation

Online material: color figures

1. MOTIVATION

It is clear that quasars are not responsible for keeping the universe ionized at redshift 6. The very brightest galaxies at those redshifts alone also provide few photons. The dominant sources of reionization so far are observationally unknown despite remarkable advances in finding sources at high redshift (e.g., Shapiro 1986; Bouwens et al. 2004; Fan et al. 2006; Thompson et al. 2007; Eyles et al. 2007) and hints for a large number of unresolved sources at very high redshifts (Spergel et al. 2007; Kashlinsky et al. 2007), which is still a topic of debate (Cooray et al. 2007; Thompson et al. 2007). At the same time, ab initio numerical simulations of structure formation in the concordance model of structure formation have found that the first luminous objects in the universe are formed inside of cold dark matter (CDM) dominated halos of total masses 2×10^5–$10^6\ M_\odot$ (Haiman et al. 1996; Tegmark et al. 1997; Abel et al. 1998). Fully cosmological ab initio calculations of Abel et al. (2000, 2002) and more recently Yoshida et al. (2006) clearly show that these objects will form isolated very massive stars. Such stars will be copious emitters of ultraviolet (UV) radiation and are as such prime suspects to get the process of cosmological reionization started. In fact, one-dimensional calculations of Whalen et al. (2004) and Kitayama et al. (2004) have already argued that the earliest H II regions will evaporate the gas from the host halos and that in fact most of the UV radiation of such stars would escape into the intergalactic medium. Recently, Yoshida et al. (2007a) and Abel et al. (2007) demonstrated with full three-dimensional radiation hydrodynamical simulations that indeed the first H II regions break out of their host halos quickly and fully disrupt the gaseous component of the cosmological parent halo. All of this gas finds itself radially moving away from the star at ~ 30 km s^{-1} at a distance of ~ 100 pc at the end of the star's life. At this time, the photoionized regions have now high electron fractions and little destructive Lyman-Werner band radiation fields creating ideal conditions for molecular hydrogen formation which may in fact stimulate further star formation above levels that would have occurred without the preionization. Such conclusions have been obtained in calculations with approximations to multidimensional radiative transfer or one-dimensional numerical models (Ricotti et al. 2002a; Nagakura & Omukai 2005; O'Shea et al. 2005; Yoshida et al. 2006; Ahn & Shapiro 2007; Johnson et al. 2007). These early stars may also explode in supernovae and rapidly enrich the surrounding material with heavy elements and deposit kinetic energy and entropy to the gas out of which subsequent structure is to form. This illustrates some of the complex interplay of star formation, primordial gas chemistry, and radiative and supernova feedback, and readily explains why any reliable results will only be obtained using full ab initio three-dimensional hydrodynamical simulations. In this paper we present the most detailed such calculations yet carried out to date and discuss issues important to the understanding of the process of cosmological reionization.

It is timely to develop direct numerical models of early structure formation and cosmological reionization as considerable efforts are underway to

1. observationally find the earliest galaxies with the *James Webb Space Telescope* (*JWST*; Gardner et al. 2006) and the Atacama Large Millimeter Array (ALMA; Wilson et al. 2005),

[1] Kavli Institute for Particle Astrophysics and Cosmology, Stanford University, Menlo Park, CA 94025.

[2] Current address: Laboratory for Observational Cosmology, NASA Goddard Space Flight Center, Greenbelt, MD 21114; john.h.wise@nasa.gov.

TABLE 1
SIMULATION PARAMETERS

Name (1)	l (Mpc) (2)	Cooling Model (3)	SF (4)	SNe (5)	$N_{\rm part}$ (6)	$N_{\rm grid}$ (7)	$N_{\rm cell}$ (8)
SimA-Adb	1.0	Adiabatic	No	No	2.22×10^7	30230	9.31×10^7 (453^3)
SimA-HHe	1.0	H, He	No	No	2.22×10^7	40601	1.20×10^8 (494^3)
SimA-RT	1.0	H, He, H_2	Yes	No	2.22×10^7	44664	1.19×10^8 (493^3)
SimB-Adb	1.5	Adiabatic	No	No	1.26×10^7	23227	6.47×10^7 (402^3)
SimB-HHe	1.5	H, He	No	No	1.26×10^7	21409	6.51×10^7 (402^3)
SimB-RT	1.5	H, He, H_2	Yes	No	1.26×10^7	24013	6.54×10^7 (403^3)
SimB-SN	1.5	H, He, H_2	Yes	Yes	1.26×10^7	24996	6.39×10^7 (400^3)

NOTE.—Col. (1): simulation name; col. (2): box size; col. (3): cooling model; col. (4): star formation; col. (5): supernova feedback; col. (6): number of dark matter particles; col. (7): number of AMR grids; col. (8): number of unique grid cells.

2. further constrain the amount and spatial nonuniformity of the polarization of the cosmic microwave background radiation (Page et al. 2007),

3. measure the surface of reionization with LOFAR (Rottgering et al. 2006), MWA (Bowman et al. 2007), GMRT (Swarup et al. 1991), and the Square Kilometer Array (SKA; Schilizzi 2004), and

4. find high-redshift gamma-ray bursts with *Swift* (Gehrels et al. 2004) and their infrared follow-up observations.

We begin by describing the cosmological simulations that include primordial star formation and accurate radiative transfer. In § 3 we report the details of the star formation environments and host halos in our calculations. Then, in § 4 we describe the resulting start of cosmological reionization, and investigate the environments in which these primordial stars form and the evolution of the clumping factor. We compare our results to previous calculations and further describe the nature of the primordial star formation and feedback in § 5. Finally, we summarize our results in the last section.

2. RADIATION HYDRODYNAMICAL SIMULATIONS

We use radiation hydrodynamical simulations with a modified version of the cosmological AMR code Enzo to study the radiative effects from the first stars (Bryan & Norman 1997, 1999). We have integrated adaptive ray tracing (Abel & Wandelt 2002) into the chemistry, energy, and hydrodynamics solvers in Enzo that accurately follow the evolution of the H II regions from stellar sources and their relevance during structure formation and cosmic reionization.

Seven different simulations are discussed here. Table 1 gives an overview of the parameters and the physics included in these calculations. We perform two cosmological realizations, simulation A (SimA) and simulation B (SimB), with three sets of assumptions about the primordial gas chemistry. The simplest calculations here assume only adiabatic gas physics and provide the benchmark against which the more involved calculations are compared. We compare this to one model with atomic hydrogen and helium cooling only and one that includes H_2 cooling. Massive, metal-free star formation is included only in the H_2 cooling models.

These calculations are initialized at redshift[3] $z = 130$ (120) when the intergalactic medium has a temperature of 325 (280) K in box sizes 1 comoving Mpc (1.5 Mpc) for SimA (SimB) with three initial nested AMR grids. We use the COSMICS package to create the initial conditions, which uses a Zel'dovich approximation (Bertschinger 1995, 2001). We use the cosmological parameters of $(\Omega_B\, h^2, \Omega_M, h, \sigma_8, n) = (0.024, 0.27, 0.72, 0.9, 1)$ from first-year *WMAP* results, where the constants have the usual meaning (Spergel et al. 2003). The changes in the third-year *WMAP* results (Spergel et al. 2007) do not affect the evolution of individual halos studied here but only delay structure formation by ~40% (Alvarez et al. 2006b). The adiabatic simulations as well as the atomic hydrogen and helium cooling only calculations are described in Wise & Abel (2007a). The new models presented here have the exact same setup and random phases in the initial density perturbation and only differ in that they include star formation as well as follow the full-radiation hydrodynamical evolution of the H II regions and supernova feedback in SimB. We use the designations RT and SN to distinguish cases in which only star formation and radiation transport were included (RT) and the one model which also includes supernovae (SN) in SimB. We use the same refinement criteria as in our previous work, where we refine if the DM (gas) density becomes 3 times greater than the mean DM (gas) density times a factor of 2^l, where l is the AMR refinement level. We also refine to resolve the local Jeans length by at least 16 cells. Cells are refined to a maximum AMR level of 12 that translates to a spatial resolution of 1.9 (2.9) comoving parsecs. This spatial resolution of ~0.1 proper pc is required to model the formation of the D-type front at small scales correctly. Refinement is restricted to the innermost initial nested grid that has a side length of 250 (300) comoving kpc.

These simulations focus on a highly biased region at $z > 15$, which could be subject to numerical artifacts created by incorrect second- and higher order growing modes (i.e., transients) associated with the Zel'dovich approximation (Scoccimarro 1998; Crocce et al. 2006). This suppresses the tails of the density and velocity probability distributions, which leads to rare events (i.e., halos) becoming less common than expected and is usually avoided by starting at very high redshifts. Although this may be the case, the halos examined in our simulations are well within cosmic variance. To illustrate this, we plot the DM halo mass function of the entire simulation volume and compare it to the one computed by an ellipsoidal variant (S-T) of the Press-Schechter formalism (Press & Schechter 1974; Sheth & Tormen 2002) in Figure 1. The circles represent the data and its associated Poisson errors, and the lines represent the S-T number densities. The halo mass function matches well with the S-T function (*solid line*) above $\sim 10^{6.5}\, M_\odot$. Below this mass, it decreases relative to the PS function because our high-resolution region samples a central box with a side $L = 250$ (300) comoving kpc. To correct for this effect, we multiply the S-T mass function by $(L/1\ {\rm Mpc})^3$ to obtain the dotted line. We chose this region because it is highly biased and should expect the halo

[3] To simplify the discussion, SimA will always be quoted first with the value from SimB in parentheses.

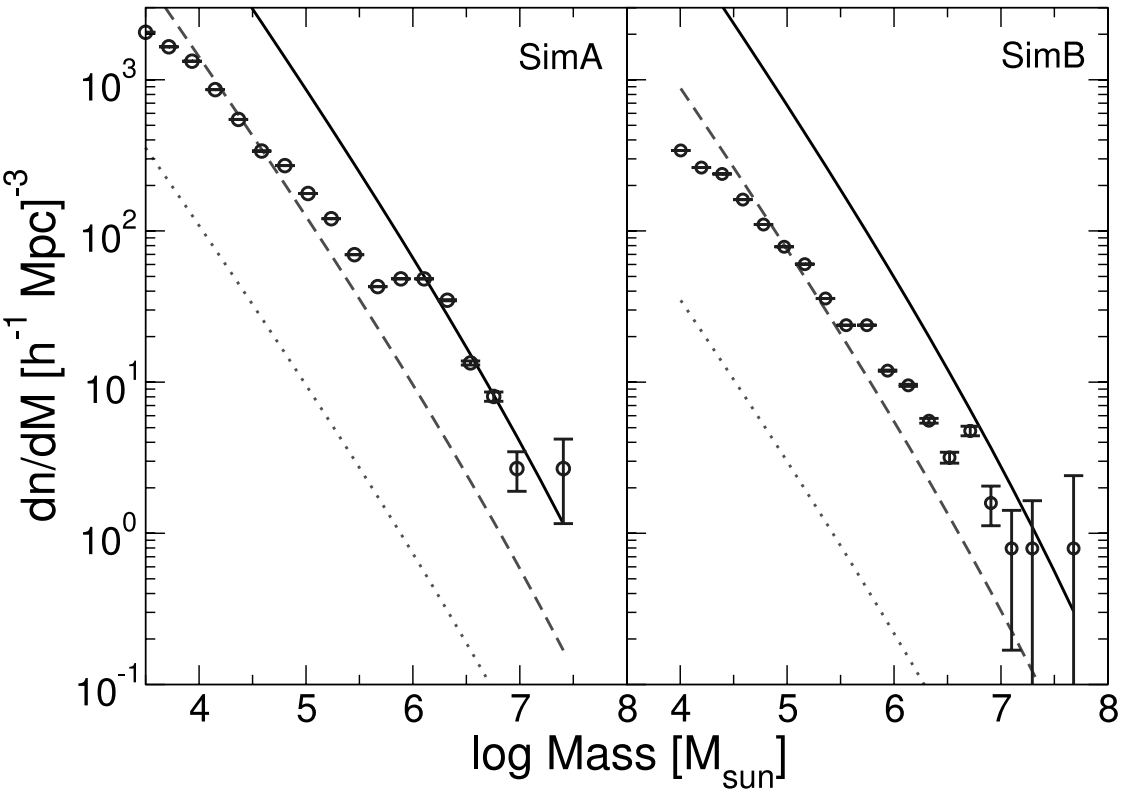

FIG. 1.—Halo mass functions for SimA at $z = 15.9$ (*left*) and B at $z = 16.8$ (*right*). The open circles are computed from the simulations. The solid line shows the halo mass function from the ellipsoidal variant of Press-Schechter formalism (Sheth & Tormen 2002). The dotted line is corrected by a factor of $(L/1\ \mathrm{Mpc})^3$, where $L = 250$ (300) kpc is the comoving length of the inner refined region. The dashed line is corrected by a factor of $b(L/1\ \mathrm{Mpc})^3$, where $b = 35$ (20) is the overdensity of halos in the biased, refined region where we allow stars to form. Our simulations agree well with the uncorrected S-T function (*solid line*) above $\sim 10^{6.5}\ M_\odot$ and the corrected function (*dashed line*) below this mass scale. [*See the electronic edition of the Journal for a color version of this figure.*]

mass function to be greater than the cosmic average. The halo mass function below $\sim 10^{6.5}\ M_\odot$ matches well with the S-T function corrected by a factor of $b(L/1\ \mathrm{Mpc})^3$, where $b = 35$ (20) is the overdensity of halos in the refined region, which is plotted as the dotted line in Figure 1. We note that recent high-resolution simulations have found that the S-T halo mass function overestimates rare objects by up to 50% at all times and halo abundances at very high redshifts (Iliev et al. 2006; Reed et al. 2007; Lukić et al. 2007). Transients from the Zel'dovich approximation used in our initial setup should not affect our general conclusions on the star formation rate and resulting reionization; however, we caution that the simulations presented here probably underestimate the clumping factor in the intergalactic medium (IGM) and number densities of low-mass halos. The effects of transients in simulations that focus on highly biased regions should be examined more carefully in the future.

The star formation recipe and radiation transport are detailed in Wise & Abel (2007c). Here we overview the basics about our method. Star formation is modeled using the Cen & Ostriker (1992) algorithm with the additional requirement that an H_2 fraction of 5×10^{-4} must exist before a star forms. We allow star formation to occur in the Lagrangian volume of the surrounding region out to three virial radii from the most massive halo at $z = 10$ in the dark matter only runs as discussed in Wise & Abel (2007a). This volume has a side length of 195 (225) comoving kpc at $z = 30$ and 145 (160) comoving kpc at the end of the calculation. The calculations with SNe use a stellar mass $M_\star$ of 170 $M_\odot$, whereas the ones without SNe use a mass of 100 $M_\odot$. The ionizing luminosities are taken from no mass loss models of Schaerer (2002) and we employ the SN energies from Heger & Woosley (2002). Star particles after the main sequence are tracked but are inert. There is evidence of lower mass primordial stars forming within relic H II regions (O'Shea et al. 2005; Yoshida et al. 2007b), but we neglect this to avoid additional uncertain parameters. This is a desired future improvement, however.

We use adaptive ray tracing (Abel & Wandelt 2002) to calculate the photoionization and heating rates caused by stellar radiation. We consider photoionization from photons with an energy of 28.4 (29.2) eV that is the mean energy of ionizing radiation from a metal-free star with 100 (170) $M_\odot$. The simulation box is large enough so that the H II region never expands outside the box; however, our ray-tracing code employs isolated boundary conditions so that photons are lost if they travel outside the computational domain. We account for H_2 photodissociation with a $1/r^2$ Lyman-Werner radiation field without self-shielding. We use a nonequilibrium, nine-species (H, H^+, He, He^+, He^{++}, e^-, H_2, H_2^+, H^-) chemistry solver in Enzo (Abel et al. 1997; Anninos et al. 1997) that takes into account the additional spatial dependence of the photoionization rates provided by the radiation transport.

We end the simulations when the most massive halo begins to rapidly collapse (i.e., $t_{\mathrm{cool}} < t_{\mathrm{dyn}}$) in the hydrogen and helium cooling only runs at redshift 15.9 (16.8). The virial temperature T_{vir} of the halo is $\sim 10^4$ K at these redshifts.

3. STAR FORMATION

Here we describe the aspects of massive metal-free star formation in our simulations. The first star forms at redshift 29.7 (30.8) in a halo typical of Population III star formation without any feedback that has a mass of $\sim 5 \times 10^5\ M_\odot$ (see Abel et al. 2000, 2002; Machacek et al. 2001; Yoshida et al. 2003, 2006). Afterward there are a total of 19, 29, and 24 instances of star formation in SimA-RT, SimB-RT, and SimB-SN, respectively.

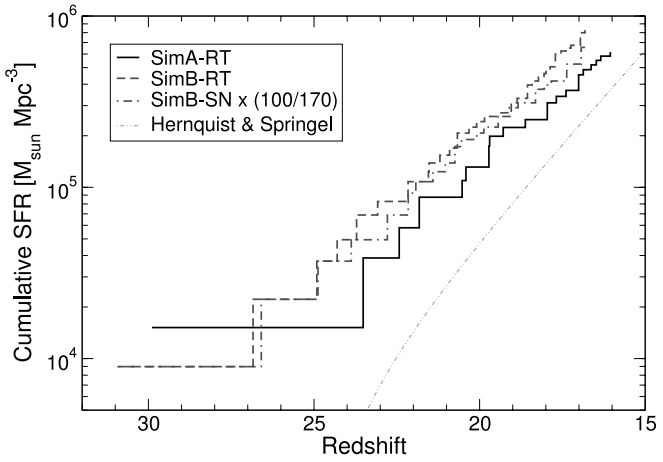

FIG. 2.—Cumulative star formation rate in units of comoving $M_\odot$ Mpc^{-3} of SimA-RT (*solid line*), SimB-RT (*dashed line*), and SimB-SN (*dot-dashed line*). The star formation rate of SimB-SN has been scaled by 100/170, which is the ratio of Population III stellar masses used in SimB-RT and SimB-SN, in order to make a direct comparison between the two simulations. The double-dotted–dashed line represents the cumulative star formation rate in atomic hydrogen cooling halos from Hernquist & Springel (2003). [*See the electronic edition of the Journal for a color version of this figure.*]

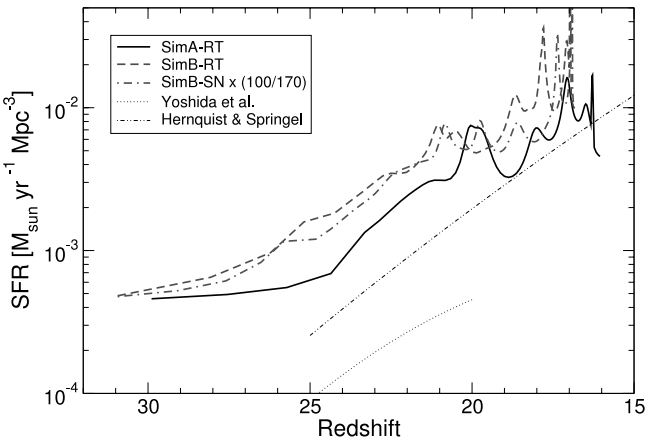

FIG. 3.—Comoving star formation rate in units of $M_\odot$ yr^{-1} Mpc^{-3}. The lines representing the simulation data have the same meaning as in Fig. 2. The crosses show at which redshifts stars form. The rates in SimB-SN are scaled for the same reason as in Fig. 2. For comparison, we overplot the star formation rates from Hernquist & Springel (2003) in atomic hydrogen line cooling halos and Yoshida et al. (2003) for 100 $M_\odot$ Population III stars. [*See the electronic edition of the Journal for a color version of this figure.*]

3.1. *Star Formation Rate*

We show the cumulative star formation rate (SFR) in units of comoving $M_\odot$ Mpc^{-3} in Figure 2. This quantity is simply calculated by taking the total mass of stars formed at a given redshift divided by the comoving volume where stars are allowed to form (see § 2). In this figure we decrease the SFR of SimB-SN by a factor of 1.7 in order to directly compare the rates from the other two simulations. This minimizes some of the uncertainties entered into our calculations when we chose the free parameter of Population III stellar mass. The cumulative rates are very similar in both realizations. The refined volume of SimA (SimB) has an average overdensity $\delta \equiv \rho/\bar{\rho} = 1.4$ (1.8). The more biased regions in SimB allow for a higher density of star-forming halos that leads to the increased cumulative SFR.

We also overplot the cumulative SFR in atomic hydrogen cooling halos from Hernquist & Springel (2003) in this figure. It is up to an order of magnitude lower than the rates seen in our calculations up to redshift 20. They only focused on larger mass halos in their simulations. The disparity between the rates is caused by our simulations only sampling a highly biased region, where we focus on a region containing a 3 σ density fluctuation, and from the contribution from Population III stars. The rates of Hernquist & Springel (2003) are calculated from an extensive suite of smoothed particle hydrodynamics simulations that encompass both large and small simulation volumes and give a more representative global SFR due to their larger sampled volumes. However, our adaptive spatial resolution allows us to study both the small- and large-scale radiative feedback from Population III stars, which is the main focus of the paper, in addition to the quantitative measures such as a SFR.

To estimate a volume-averaged SFR (i.e., Madau et al. 1996 in units of comoving $M_\odot$ yr^{-1} Mpc^{-3}) from the cumulative SFR, we need to smooth the discretely increasing cumulative SFR to ensure its time derivative (i.e., the SFR) is a smoothly varying function. Otherwise, the SFR would be composed of delta functions when each star forms. We first fit the cumulative SFR with a cubic spline with 10 times the temporal resolution. Then we smooth the data back to its original time resolution and evaluate its time derivative to obtain the SFR that we show in Figure 3. We also mark the redshifts of star formation with crosses. We again compare our rates to ones calculated in Hernquist & Springel (2003) for metal-enriched stars and Yoshida et al. (2003) for Population III stars with a mass of 100 $M_\odot$. Our rates are higher for reasons discussed previously. We do not advocate these SFRs as cosmic averages but give them as a useful diagnostic of the performed simulations.

We see an increasing function from 5×10^{-4} $M_\odot$ yr^{-1} Mpc^{-3} at redshift 30 to $\sim 6 \times 10^{-3}$ $M_\odot$ yr^{-1} Mpc^{-3} at redshift 20. Here only one star per halo forms in objects with masses $\lesssim 5 \times 10^6$ $M_\odot$. Above this mass scale, star formation is no longer isolated in nature and can be seen by the bursting nature of the star formation after redshift 20, where the SFR fluctuates around 10^{-2} $M_\odot$ yr^{-1} Mpc^{-3} (see Ricotti et al. 2002b). Since we neglect H_2 self-shielding, the strong Lyman-Werner (LW) radiation dissociates almost all H_2 in the host halo and surrounding regions. Thus we rarely see simultaneous instances of star formation. However, the regions that were beginning to collapse when a nearby star ignites form a star 3–10 million years after the nearby star dies. This only results in a minor change in the timing of star formation. Furthermore this delay is minimal compared to the Hubble time and does not affect SFRs.

3.2. *Star-forming Halo Masses*

We show the star formation times versus the host halo DM masses as a function of redshift in Figure 4. The DM halo masses are calculated with the HOP algorithm (Eisenstein & Hut 1998). First we focus on star formation in the largest halo. Around redshift 30, the first star forms in all three simulations with a mass of $\sim 5 \times 10^5$ $M_\odot$. The stellar radiation drives a $\sim$30 km s^{-1} shock wave that removes almost all of the gas from the shallow potential well. It takes approximately 75 (40) million years for gas to reincorporate into the potential well from smooth IGM accretion and mergers. At $z \sim 24$ in SimB-RT, the second star forms in the most massive progenitor that now has a mass of 4×10^6 $M_\odot$. In SimA-RT, the merger history is calmer at $z = 24$–30, and enough gas becomes available for H_2 cooling and star formation at $z \sim 20$. Here the second star forms in the most massive progenitor that has a mass of 5×10^6 $M_\odot$. In both RT simulations, the stellar feedback expels most of the gas from its host once again. For SimA (SimB), another 10 (30) million years pass before the next star

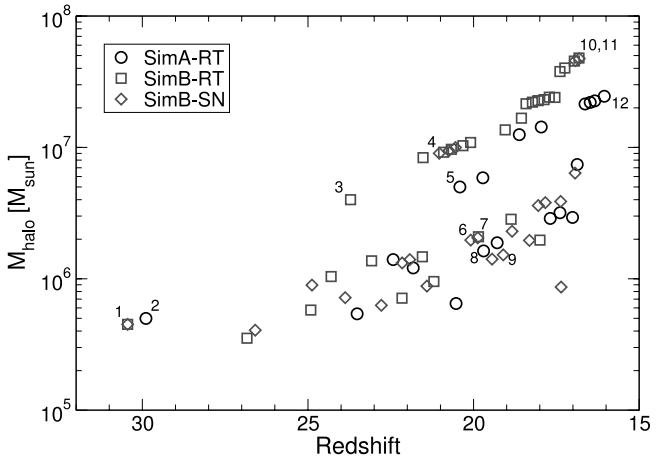

FIG. 4.—Star formation times vs. host halo DM mass for SimA-RT (*circles*), SimB-RT (*squares*), and SimB-SN (*triangles*). One symbol represents one star. The numbers correspond to the halo numbers listed in Table 2. [*See the electronic edition of the Journal for a color version of this figure*.]

forms in this halo. Once the halo has a mass of $\sim 10^7\,M_\odot$, the potential energy is great enough to confine most of the stellar and SNe outflows. In SimA-RT and SimB-RT, halos above this mass scale host multiple sites of star formation that is seen in the nearly continuous bursts of star formation in the most massive halo. SimA-RT forms stars more intermittently than SimB-RT because it undergoes two major mergers between redshift 17 and 21 (see Wise & Abel 2007a). In SimB-SN at $z = 21$, three stars form in succession in the most massive halo. Their aggregate stellar and SNe feedback expels the gas from its halo one more time. This halo only forms another star at $z = 16.9$ (55 million years later) in this halo when enough gas has been reincorporated.[4]

Most of the stars form in low-mass halos with masses $\sim 10^6\,M_\odot$ that are forming its first star between redshifts 18–25 in our calculations. A slight increase in host halo masses with respect to redshift mainly occurs because of the negative feedback from photoevaporation of low-mass halos that are close to other star-forming halos (Haiman et al. 2001). Additional delays in star formation may be caused by ultraviolet heating and H_2 dissociation from previous stars (e.g., Machacek et al. 2001; Yoshida et al. 2003; Mesinger et al. 2006), which increase the critical halo mass in which gas can cool and condense.

One interesting difference in SimB-SN from the other calculations is that star formation is sometimes induced in overdensities within the same halo when a SN blast wave overtakes it. This occurs in three halos with masses of 2.0, 1.5, and $3.8 \times 10^6\,M_\odot$ at redshifts 19.9, 19.1, and 17.8, respectively. The same halos in SimB-RT do not form two stars before their gas is expelled, thus quenching subsequent star formation.

3.3. *Star Formation Environments*

We further study the nature of high-redshift star formation by selecting four star-forming regions from each simulation and studying the surrounding interstellar medium (ISM) prior to star formation. The ISM in the 10^4 K halos is described in more detail in Wise & Abel (2007c). The sample of regions are chosen in order to compare different star formation environments. These regions can be categorized into (1) first star inside an undisturbed halo, (2) first star that is delayed by LW radiation, (3) induced star formation by positive feedback, (4) star formation after gas reincorporation, and (5) star formation in a halo with a virial temperature over 10^4 K. The represented halos and their parameters are listed in Table 2 and annotated in Figure 4.

We plot the mass-weighted radial profiles of number density (left columns) and temperature (right columns) within the virial radius for these 12 halos in Figure 5 and describe them below.

1. *First star* (*halos 1, 2*).—These stars are the first to form in their respective simulation volume. The structures of the host halos within our resolution limit exhibit similar characteristics, e.g., a self-similar collapse and central temperatures of 300 K, as in previous studies (Abel et al. 2000, 2002; Bromm et al. 2002; Yoshida et al. 2006). The halo masses are $4.8(4.7) \times 10^5\,M_\odot$. Heating from virialization raises gas temperatures to 3000 K, and in the central parsec, H_2 cooling becomes effective and cools the gas down to 200 K, which drives the further collapse. The mass-weighted central gas densities and temperatures are approximately 3000 cm^{-3} and 320 K, respectively.

2. *Delayed first star* (*halos 6, 7, 8*).—The host halos have similar radial profiles as the halos that hosted the first stars but with

[4] We have run SimB-SN past $z = 16.8$ and have seen that it starts to host multiple sites of star formation.

TABLE 2
SELECTED STAR-FORMING HALO PARAMETERS

Number (1)	Simulation (2)	Type (3)	z (4)	M_{vir} ($M_\odot$) (5)	f_b (6)	ρ_c (cm^{-3}) (7)	T_c (K) (8)
1	SimB-RT	1	30.9	4.7×10^5	0.081	1600	340
2	SimA-RT	1	29.9	4.8×10^5	0.094	6500	350
3	SimB-RT	4	23.7	5.3×10^6	0.059	2400	410
4	SimB-SN	4	21.0	1.1×10^7	0.045	1800	480
5	SimA-RT	4	20.4	6.3×10^6	0.069	550	440
6	SimB-SN	2	20.1	2.6×10^6	0.12	120	390
7	SimB-RT	2	19.9	2.8×10^6	0.12	870	450
8	SimA-RT	2	19.3	2.9×10^6	0.13	1300	440
9	SimB-SN	3	19.3	2.3×10^6	0.12	360	450
10	SimB-RT	5	16.8	3.1×10^7	0.089	4100	2500
11	SimB-SN	5	16.8	2.9×10^7	0.065	1100	590
12	SimA-RT	5	16.1	3.0×10^7	0.061	130	470

NOTE.—Col. (1): halo number; col. (2): simulation source; col. (3): star formation type; col. (4): redshift; col. (5): virial mass; col. (6): baryon mass fraction; col. (7): central number density; col. (8): central temperature.

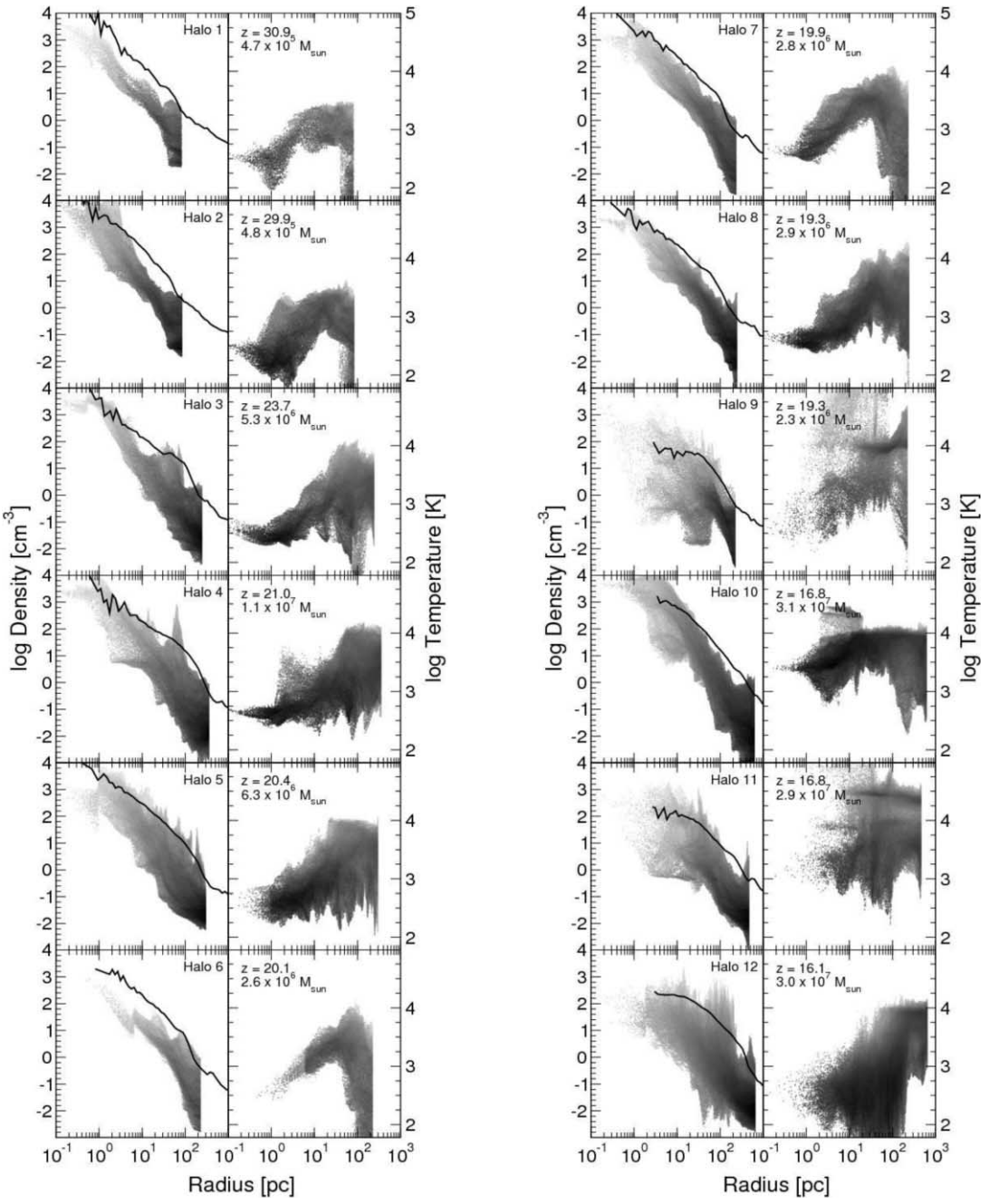

FIG. 5.—Radial profiles of number density (*left column*) and temperature (*right column*) for selected star-forming halos inside the virial radius. We overplot the radially averaged DM density (*solid line*) in units of m_h cm^{-3}. These data represent the state of the region immediately after star formation. Notice the added complexity (range) in the density and temperature with increasing host halo mass, especially if the region has been affected by stellar radiation, as in halos 3, 4, 5, 10, 11, and 12. The occasional discontinuities in density in the inner parsec arise from our star formation recipe when we remove half the mass in a sphere containing twice the stellar mass.

masses of $\gtrsim 10^6\,M_\odot$. Here the H_2 cooling has been stifled by the LW radiation from nearby star formation. Only when the halo mass passes a critical mass can the core cool and condense by H_2 formation (Machacek et al. 2001; Yoshida et al. 2003; O'Shea & Norman 2007; Wise & Abel 2007b). The central densities are lower than the first stars with 1300, 870, and 120 cm^{-3} in SimA-RT, SimB-RT, and SimB-SN, respectively. The central temperatures are marginally higher at 440, 450, and 390 K.

3. *Induced star formation* (*halo 9*).—At $z = 19.3$, a massive star explodes in a SN, whose shell initially propagates outward at 4000 km s^{-1}. After 160 kyr, the shell passes an overdensity within the same halo that is caused by an ionization front instability (e.g., see Whalen & Norman 2008a, 2008b). The star forms 35 pc away from the SN explosion and the DM halo center. The combination of the shock passage and excess free electrons in the relic H II catalyze H_2 formation in this low-mass halo (e.g., Ferrara 1998; O'Shea et al. 2005; Mesinger et al. 2006). The SN blast wave heats the gas over 10^4 K to radii of 1 pc. In the density profile, both low- and high-density gas exists at similar radii. Here the shock passage creates a tail of gas streaming from the central core, whose asymmetries can be seen in the density profile. However, the core survives and benefits from the excess electrons created during this event. The central temperature is similar to the previous cases at 450 K. The H_2 criterion for star formation is reached faster because of the excess electrons, which creates a star particle at a lower density (360 cm^{-3}).

4. *Star formation after reincorporation* (*halos 3, 4, 5*).—After a sufficient amount of gas that was expelled by dynamical feedback of the first star is reincorporated into the halo, star formation is initiated again. Here virial temperatures of the halos are under 10^4 K, which are hosting their second instance of star formation. These halos have a larger spread in gas densities and temperatures than the halos forming their first star. Gas is heated by virialization and prior stellar radiation to over 10^4 K outside 10 pc. The central densities in halos 3 and 5 are similar to the regions described in the first star formation section; however, they are slightly warmer at 410 and 480 K. Halo 4 shows a more diffuse core with densities of 550 cm^{-3} and temperatures of 440 K.

5. *Star formation in* 10^4 K *halos* (*halos 10, 11, 12*).—In these halos, H_2 formation is aided by atomic hydrogen cooling. The ISM becomes increasingly complex as more stars form in the halo. The temperatures range from 100 to 20,000 K throughout the halo. Halos 10 and 12 have hosted 16 and 8 massive stars, respectively, since they started to continually form stars at $z \sim 20$. In SimB-RT (halo 10), the densities are higher than in these cases. The gas in this halo is more centrally concentrated than the others because the H II regions did not break out of the halo, thus minimizing any outflows from feedback and dispersion of the central core. The temperature in halo 10 is significantly warmer than other regions, at 2500 K. In halo 11, the devastation caused by three stars and their SNe at $z = 21$ prevented star formation until $z = 16.9$. Its initial recovery from that event is apparent by the single cool core with a temperature of 590 K that sharply transitions to a warm, diffuse medium at $r = 10$ pc. Halo 12 (SimA-RT) has a complex morphology that is not centrally concentrated and is caused by stellar outflows during a major merger (see Wise & Abel 2007c for images). This morphology manifests itself in the radial profiles as large density contrasts spanning nearly 6 orders of magnitude at $r = 30$–300 pc. Similarly, temperatures range from 50 to 10,000 K in the same region. The star forms in a diffuse region ($\rho = 130$ cm^{-3}) that has a temperature of 470 K and whose H_2 formation is enhanced because it resides in a relic H II region.

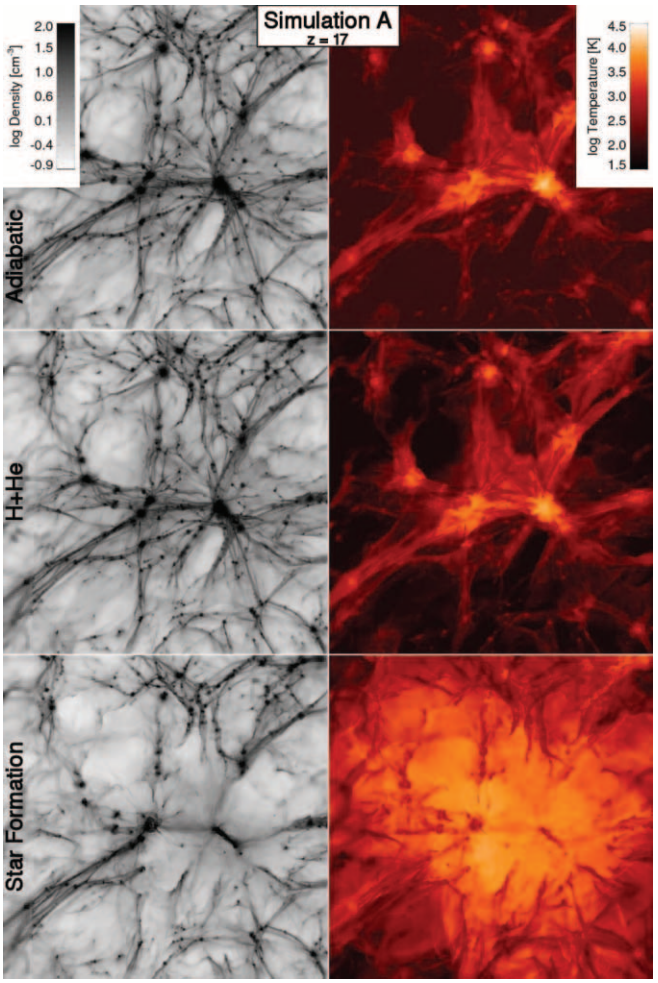

FIG. 6.—Density-squared weighted projections of gas density (*left*) and temperature (*right*) of SimA. The field of view is 8.5 proper kpc (1/216 of the simulation volume) and the color scale is the same for all simulations.

4. STARTING COSMOLOGICAL REIONIZATION

In this section we first describe the ionizing radiation from massive stars that start cosmological reionization in small overdense regions we simulate. Then we discuss the effects of recombinations in the inhomogeneous IGM and kinetic energy feedback from Population III stars. Lastly, the evolution of the average IGM thermal energy is examined.

To illustratively demonstrate radiative feedback from massive stars on the host halos and IGM, we show projections of gas density and temperature that are density-squared weighted in Figures 6 and 7 for all of the simulations at redshift 17. These projections have the same field of view of 8.5 proper kpc and the same color maps. The large-scale density structure is largely unchanged by the stellar feedback, and the adjacent filaments remain cool since they are optically thick to the incident radiation. H_2 cooling produces more centrally concentrated objects; however, stellar feedback photoevaporates $\lesssim 10^6\,M_\odot$ halos near other star-forming halos. This is apparent in the density projections in the Jeans smoothing around the most massive halo (see Haiman et al. 2001; Mesinger et al. 2006). Kinematic feedback from SNe has an even larger effect on the surrounding gas. In SimB-SN, this effect is seen in the reduced small-scale structure and low-mass halos with no gas counterparts. However, the most apparent difference in the radiative simulations is the IGM heating by Population III stars, especially in SimB-SN.

4.1. *UV Emissivity*

A key quantity in reionization models is volume-averaged emissivity of ionizing radiation. We utilize the comoving SFR $\dot{\rho}_\star$ to calculate the proper volume-averaged UV emissivity,

$$\epsilon = \frac{\dot{\rho}_\star Q_{\rm H\,I} t_{\rm H}}{\bar{\rho}_b}, \tag{1}$$

in units of ionizing photons per baryon per Hubble time. Here $Q_{\rm H\,I}$ is the number of ionizing photons emitted in the lifetime of a star per solar mass, $\bar{\rho}_b \simeq 2 \times 10^{-7}$ is the comoving mean number density, and

$$t_{\rm H} \approx \frac{2}{3H_0\sqrt{\Omega_m}}(1+z)^{-3/2} \tag{2}$$

is the Hubble time in an Einstein–de-Sitter universe, which is valid for ΛCDM cosmology at $z \gg 1$. For Population III stellar masses greater than 100 $M_\odot$, $Q_{\rm H\,I} \approx 10^{62}$ photons per solar mass, corresponding to 84,000 ionizing photons per stellar proton (Schaerer 2002). We plot the emissivity ϵ in Figure 8*a*. It follows the same behavior as the SFR, but now can be directly used in semianalytic reionization models. The emissivity increases from unity at redshift 30 to ~100 at the end of our simulations. Our results agree with the emissivity calculated in semianalytic models

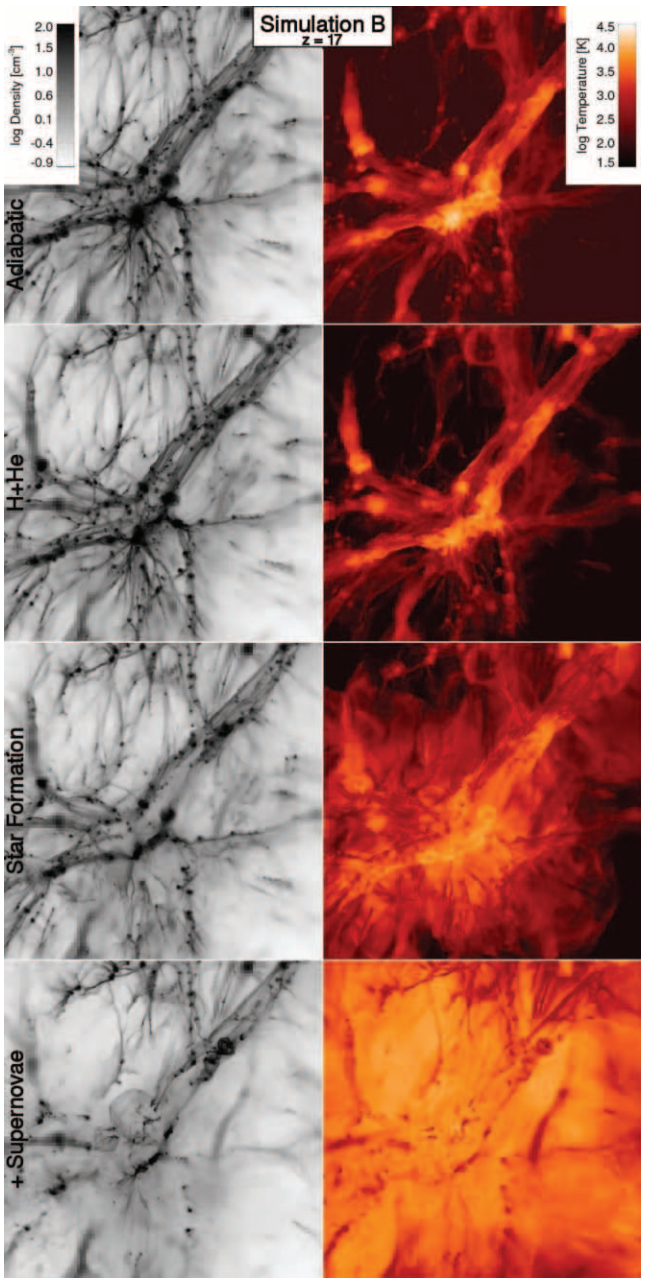

FIG. 7.—Same as Fig. 6, but for SimB.

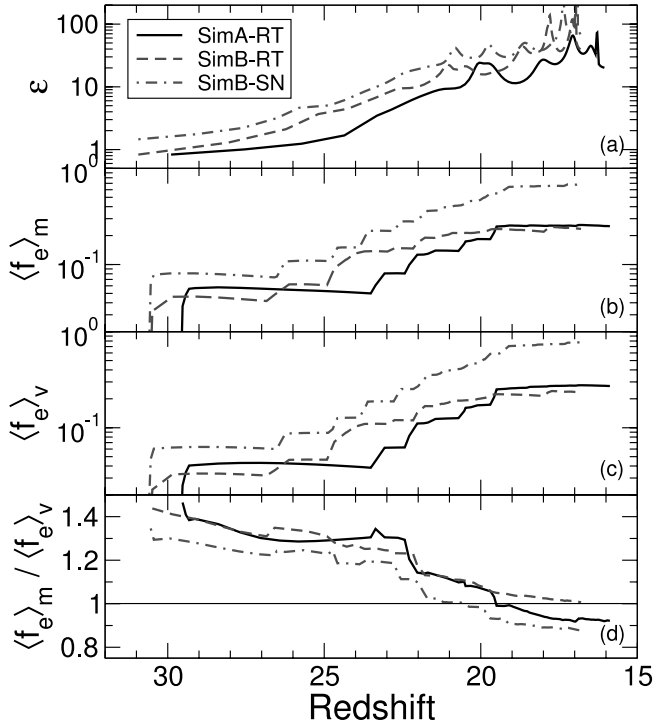

FIG. 8.—(*a*) Averaged emissivity in units of ionizing photons per baryon per Hubble time that is calculated from the star formation rate in Fig. 3. (*b*) Mass-averaged ionization fraction ($f_e > 10^{-3}$) of the inner 250 (300) comoving kpc for SimA (SimB). (*c*) Volume-averaged ionization fraction for the same runs. (*d*) The ratio of the mass- and volume-averaged ionization fraction. [*See the electronic edition of the Journal for a color version of this figure.*]

that include Population III stars (e.g., Onken & Miralda-Escudé 2004) and should be an upper limit however.

4.2. *Effective Number of Ionizations per UV Photon*

We show the mass-averaged and volume-averaged ionization fraction f_e within the refined region in Figure 8*b* and 8*c*. The ratio of these fractions are plotted in Figure 8*d*. The first star in the simulation ionizes between 5% and 10% of the volume where we allow star formation. As stars begin to form in other halos after redshift 25, the ionization fraction gradually builds to 30% in the RT simulations and 75% in the SN case. The higher stellar luminosities in SimB-SN, which can be seen in Figure 8*a*, and the additional outflows generated by SN blast waves cause this difference in f_e. The ratio $\langle f_e \rangle_m / \langle f_e \rangle_v$ illustrates that the ionized regions are overdense by a factor of ~1.25 at early times in the simulation, but then decreases to unity as the H II region grows. In addition, the H II regions in halos with sustained star formation in the RT simulations do not fully break out into the IGM. Kitayama et al. (2004) provided a useful approximation of the critical halo mass

$$M_{\rm crit}^{\rm ion} \sim 2.5 \times 10^6 \left(\frac{M_\star}{200\ M_\odot} \right)^{3/4} \left(\frac{1+z}{20} \right)^{-3/2} M_\odot, \qquad (3)$$

in which an ionization front (I-front) cannot escape. This approximation is valid for stellar masses between 80 and 500 $M_\odot$, redshifts between 10 and 30, and singular isothermal spheres. Our simulations exhibit this same trait in which I-fronts only partially break out from the host halo above this mass scale.

This is not the case with SNe because previous SN blast waves can more effectively evacuate the surrounding medium, thus increasing the chances of radiation escaping into the IGM from later stars in the same halo. At $z = 21$, there is an example of this occurring with three stars forming in succession in the most massive halo. After the first star goes SN, a diffuse and hot medium is left behind, but the blast wave has not completely disrupted two other nearby condensing clumps. The radiation from the second star now does not have to ionize its host halo and has an escape fraction of near unity. The same happens for the third star in this halo. This episode further ionizes SimB-SN from 40% to 60%. As a note of caution, these ionized fractions should not be considered as cosmological average because they only sample a highly biased region. Iliev et al. (2006) showed that a simulation box size of ~30 Mpc is needed to make global predictions.

To examine the strength of recombinations, we compare the total number of electrons in the volume to the total number of ionizing photons emitted in Figure 9. The ratio of these two quantities is the number of UV photons needed for one effective ionization initially. This ratio is approximately 3/5 (1/3) after the first star dies. The values in SimA are higher due to its smaller

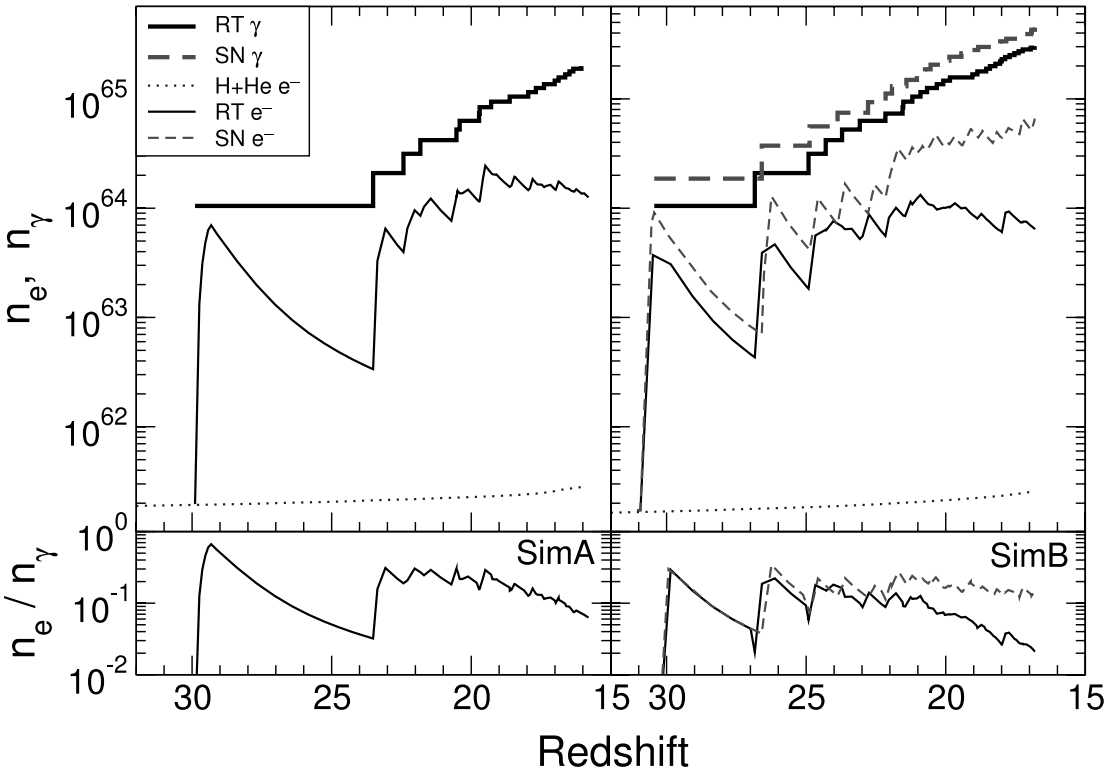

FIG. 9.—*Top panels*: Total number of ionizing photons emitted (*thick lines*) and total number of electrons (*thin lines*) for simulations with cooling only (*dotted lines*), star formation only (*solid lines*), and supernovae (*dashed lines*) in the inner 250 and 300 comoving kpc for SimA (*left*) and SimB (*right*). The H II regions are completely contained in these volumes. *Bottom panels*: The ratio of total number of electrons to the total number of ionized photons emitted. [*See the electronic edition of the Journal for a color version of this figure.*]

volume. This ratio then steadily decreases from recombinations in the relic H II region to a few percent when the next star forms. As stars begin to form regularly in the simulation, there are 4 (6) photons per sustained ionization. However, this ratio drops by a factor of 5 in the RT simulations after $z \sim 20$ when the H II regions become trapped in the halo, thus reducing the available photons for ionizing the IGM. The effects of SNe as previously discussed maintain the ratio of 6 photons required per ionization as the most massive halo grows in mass.

4.3. *Clumping Factor Evolution*

Volume-averaged recombination rates in an inhomogeneous IGM scale with the clumping factor $C = \langle \rho^2 \rangle / \langle \rho \rangle^2$, where the angle brackets denote volume-averaged quantities. The recombination rate for hydrogen, e.g., is simply

$$\left(\frac{dn_{\rm H\,II}}{dt} \right)_{\rm rec} = C k_{\rm rec} f_e \bar{\rho}_b (1+z)^3, \qquad (4)$$

where $k_{\rm rec}$ is the case B recombination rate for hydrogen at $T \approx 10^4$ K, and $f_e = n_e/n$ is the ionization fraction. Both the increased recombinations in overdense regions and photon escape fractions lower than unity result in the high number of UV photons needed for one effective ionization that we see in our simulations.

Figure 10 compares the clumping factor in the adiabatic, cooling only, star formation, and supernova calculations, which we separate into C for all gas (*thin lines*) and ionized gas (*thick lines*). Since we resolve the local Jeans length by at least four cells in all simulations, the clumping factor is not underestimated, given our assumptions about gas cooling in each model. Recall that our simulations use the Zel'dovich approximation for the initial conditions, which may lead to underestimating the clumping factor. We do not include dense ($\delta > 100$) gas, residing in filaments and halos, in the clumping factor calculation as we restrict this analysis to the IGM because these overdensities are self-shielded from incident ionizing radiation (e.g., Shapiro et al. 1997, 2004; Iliev et al. 2005; Whalen et al. 2008).

The clumping factor in the adiabatic and cooling-only cases smoothly increases to $\sim$5 at $z = 17$ from unity at $z > 30$. The clumping factor in the star formation and supernova simulations are smaller by 10%–25% than the other simulations because the overdensities in the IGM are photoevaporated by the nearby stars. SN explosions disperse gas more effectively than radiative feedback alone in larger halos and can have a bigger impact on the clumping factor. At redshift 20, the three stars and their SN energy in the most massive halo destroy the surrounding baryonic structures and reduce the clumping back to the values seen in nonradiative cases.

We plot the clumping factor $C_{\rm ion}$ in ionized regions above $x_e > 10^{-3}$ as the thick lines in Figure 10. This value is most relevant for recombination rates. Around the first star in the simulation, the IGM is overdense and contains larger amounts of clumps than the rest of the simulation. This increased clumpiness competes with photoevaporation caused by the nearby star to create $C_{\rm ion}$ values that are comparable to C for all gas at $z > 25$. Afterward $C_{\rm ion}$ is always smaller than C with a maximum decrease of $\sim$25%.

4.4. *Kinetic Energy Feedback*

SN explosion energy and kinetic energy generated in D-type I-fronts play a key role in star formation in low-mass halos, which are easily affected due to their shallow potential well (e.g., Dekel & Silk 1986; Haehnelt 1995; Bromm & Loeb 2003; Whalen et al. 2004; Kitayama et al. 2004; Kitayama & Yoshida 2005). The

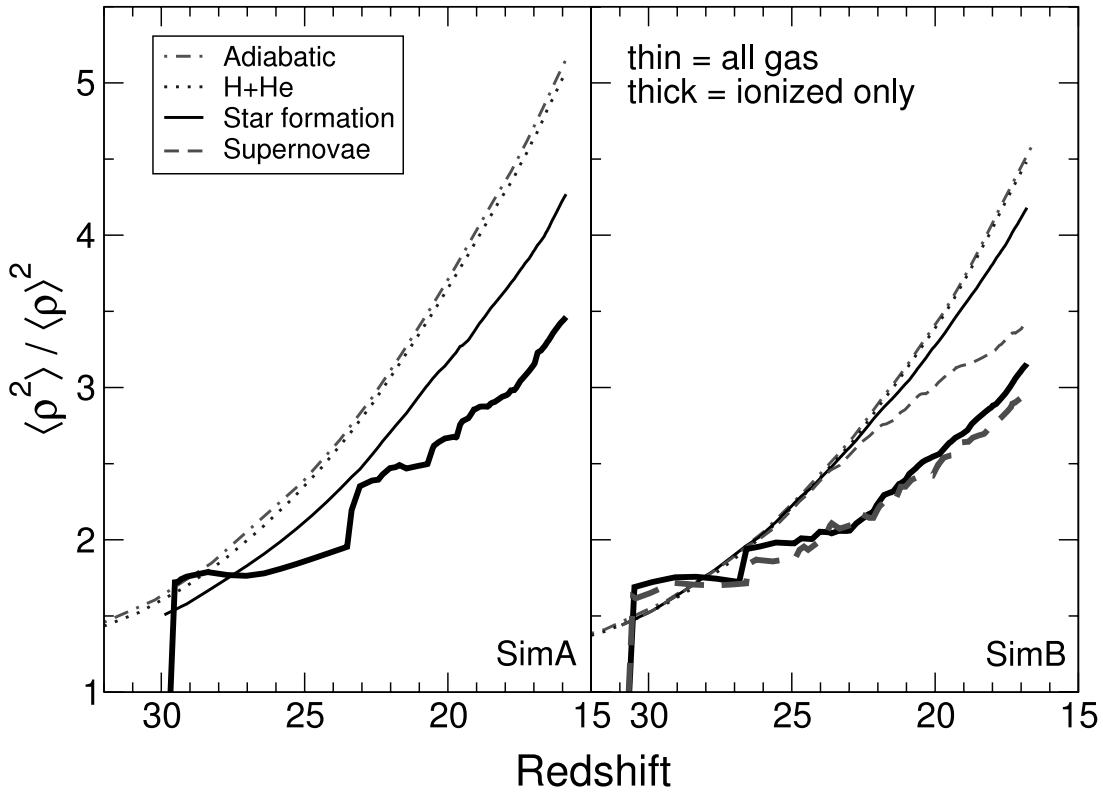

FIG. 10.—Clumping factor $C = \langle\rho^2\rangle/\langle\rho\rangle^2$ for SimA (*left*) and SimB (*right*), comparing the cases of the adiabatic equation of state (*dot-dashed line*), atomic hydrogen and helium cooling (*dotted line*), star formation only (*solid line*), and supernovae (*dashed line*). The clumping factors for all diffuse ($\delta < 100$) gas are plotted as thin lines, and the clumping factors for ionized, diffuse gas, $C_{\rm ion}$, are plotted as thick lines. [*See the electronic edition of the Journal for a color version of this figure.*]

kinetic energy created by SNe is sufficient to expel the gas from these low-mass halos. For example, the binding energy of a $10^6\,M_\odot$ halo is only 2.8×10^{50} ergs at $z = 20$, which is 2 orders of magnitude smaller than the typical energy output of a pair instability SN (Heger & Woosley 2002). For a $T_{\rm vir} > 10^4$ K halo at the same redshift, it is 9.4×10^{52} ergs. With our chosen stellar mass of 170 $M_\odot$, it takes 3–4 SNe to overcome this potential energy.

The shock wave created by the D-type I-front travels at a velocity $v_s = 25$–$35\ {\rm km\ s^{-1}}$ for density gradients [i.e., $\rho(r) \propto r^{-w}$] with slopes between 1.5 and 2.25 (Shu et al. 2002; Whalen et al. 2004; Kitayama et al. 2004). This velocity is the escape velocity for halos with masses greater than $3 \times 10^8\ M_\odot$ at $z = 15$, which is an order of magnitude greater than the most massive halos studied here. However, less massive halos can contain these I-fronts because pressure forces slow the I-front after the star dies.

Using the position of the shock wave when the star dies (eq. [6]) and energy arguments, we can estimate the critical halo mass where the material in the D-type I-front can escape from the halo by comparing the binding energy E_b of the halo and kinetic energy in the shell. For most massive stars, the shock wave never reaches the final Strömgren radius,

$$R_{\rm str} = 150\left(\frac{\dot{N}_{\rm H\,I}}{10^{50}\ {\rm photons\ s^{-1}}}\right)^{1/3}\left(\frac{n_f}{1\ {\rm cm^{-3}}}\right)^{-2/3}\ {\rm pc}, \quad (5)$$

before the star dies. Here $\dot{N}_{\rm H\,I}$ is the ionizing photon rate of the star, and n_f is the average number density of gas contained in this radius. After the lifetime of the star, the shock reaches a radius

$$R_s = 83\left(\frac{v_s}{30\ {\rm km\ s^{-1}}}\right)\left(\frac{t_\star}{2.7\ {\rm Myr}}\right)\ {\rm pc}, \quad (6)$$

where $t_\star$ is the stellar lifetime (see also Kitayama et al. 2004). We can neglect isolated, lower mass ($M \lesssim 30\ M_\odot$) Population III stars whose shock wave reaches $R_{\rm str}$ within its lifetime. In this case, the I-front stops at $R_{\rm str}$, and the shock wave becomes a pressure wave that has no associated density contrast in the neutral medium (Shu 1992). Thus we can safely ignore these stars in this estimate.

Assume that the source is embedded in a single isothermal sphere. The mass contained in the shell is

$$M_{\rm sw} = \frac{(\Omega_b/\Omega_M)M_{\rm vir}R_s}{r_{\rm vir}} - V_s\rho_i, \quad (7)$$

which is the mass enclosed in the radius R_s in an isothermal sphere, corrected for the warm, ionized medium behind the I-front. Here V_s is the volume contained in a sphere of radius R_s, and ρ_i is the gas density of the ionized medium, whose typical number density is 1 $\rm cm^{-3}$ for stellar feedback from a massive primordial star (Whalen et al. 2004; Kitayama et al. 2004; Yoshida et al. 2007a; Abel et al. 2007). For massive stars ($M_\star \gtrsim 30\ M_\odot$), the mass of the central homogeneous medium is small (i.e., 10%) compared to the shell. We compensate for this interior mass by introducing the fraction η, so the shell mass is simply

$$M_{\rm sw} = \eta\frac{(\Omega_b/\Omega_M)M_{\rm vir}r_s}{r_{\rm vir}}. \quad (8)$$

For these outflows to escape from the halo, the kinetic energy contained in the shell must be larger than the binding energy, which is

$$\frac{1}{2}M_{\rm sw}v_s^2 > \frac{GM_{\rm vir}^2}{2r_{\rm vir}}. \quad (9)$$

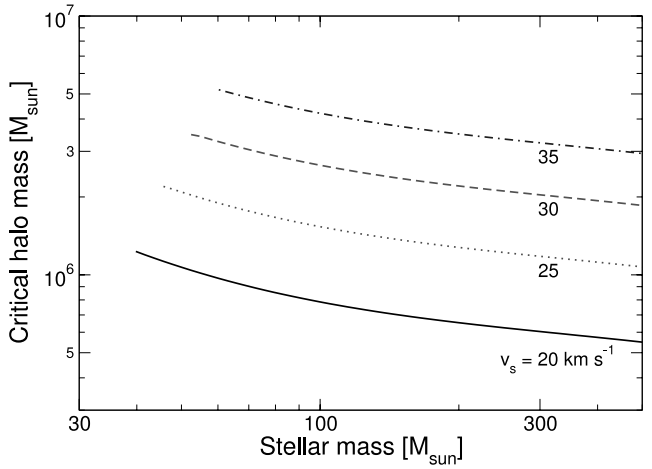

FIG. 11.—Maximum halo mass in which a D-type ionization front can create outflows as a function of primordial stellar mass for shock velocities v_s of 20, 25, 30, and 35 km s^{-1}. Here the fraction η of mass contained in the shell is 0.9. [*See the electronic edition of the Journal for a color version of this figure.*]

Using equations (6) and (8) in this condition, we obtain the maximum mass

$$M_{\rm max} \sim \frac{r_s v_s^2 \Omega_b}{G\Omega_M},$$

$$M_{\rm max} \sim 3.20\times10^6 \left(\frac{r_s}{100\ {\rm pc}}\right)\left(\frac{v_s}{30\ {\rm km\ s^{-1}}}\right)^2 \times \left(\frac{\eta}{0.9}\right)\left(\frac{\Omega_b/\Omega_M}{0.17}\right) M_\odot \quad (10)$$

of a halo where the material in the shock wave becomes unbound, expelling the majority of the gas from the halo.

In Figure 11 we use the stellar lifetimes and ionizing luminosities from Schaerer (2002) to calculate the critical halo mass for outflows for stellar masses 5–500 $M_\odot$ and for shock velocities of 20, 25, 30, and 35 km s^{-1} with $\eta = 0.9$. For stellar masses smaller than 30 $M_\odot$, the D-type I-front reaches the final Strömgren sphere and cannot expel any material from the host. Hence they are not plotted in this figure. For the more massive stars, the star dies before the D-type I-front can reach the Strömgren radius, thus being limited by $t_\star$. This maximum halo mass is in good agreement with our simulations as we see halos with masses greater than $5\times10^6\ M_\odot$ retaining most of their gas in the star formation only cases. However, in larger halos, stellar sources still generate champagne flows, but this material is still bound to the halo and returns in tens of millions of years.

4.5. *Thermal Energy*

Thermal feedback is yet another mechanism how Population III stars leave their imprint on the universe. The initial heating of the IGM will continue and intensify from higher SFRs at lower redshifts (e.g., Hernquist & Springel 2003; Onken & Miralda-Escudé 2004). It is possible to constrain the reionization history by comparing temperatures in the Lyα forest to different reionization scenarios (Hui & Haiman 2003). Temperatures in the Lyα forest are approximately 20,000 K at $z = 3$–5 (Schaye et al. 2000; Zaldarriaga et al. 2001). Although our focus was not on redshifts below 15 due to the uncertainty of the transition to the first low-mass metal-enriched (Population II) stars, we can utilize the thermal data in our radiation hydrodynamical simulations to infer the thermal history of the IGM at lower redshifts.

The excess energy from hydrogen ionizing photons over 13.6 eV photoheats the gas in the H II region. The mean temperature within H II regions in our calculations is ~30,000 K. When the short lifetime of a Population III star is over, the H II region cools mainly through Compton cooling off the cosmic microwave background. The same framework applies to SNe remnants as well. The timescale for Compton cooling is

$$t_{\rm C} = 1.4\times10^7 \left(\frac{1+z}{20}\right)^{-4} f_e^{-1}\ {\rm yr}. \quad (11)$$

This process continues until the gas recombines, and Compton cooling is no longer efficient because of its dependence on electron fraction. Radiation preferentially propagates into the voids and leaves the adjacent filaments and its embedded halos virtually untouched. Hence we can restrict the importance of Compton cooling to the diffuse IGM since Compton cooling cools the gas to low temperatures without being impeded by recombinations that are proportional to n_e^2. This causes the relic H II region to cool to temperatures down to 300 K. The temperature evolution in our radiative calculations agrees with the analytic models of relic H II (Oh & Haiman 2003).

We plot the volume-averaged temperature $\langle T\rangle_v$ and mass-averaged temperature $\langle T\rangle_m$ in the volume where we allow star formation, i.e., the inner 250 (300) comoving kpc, in Figures 12 and 13. We compute the average temperatures in both neutral and ionized ($f_e > 10^{-3}$) regions. We first focus on the thermal evolution of neutral gas. An increase of the average temperature in neutral gas is indicative of heating by hard photons or supernovae. At the final redshift $z = 16.8$, $\langle T\rangle_v = 180$ K in neutral gas with SNe compared with 90 K without SNe. Both of these average temperatures are a factor of 2–3 higher than without star formation. With SNe, $\langle T\rangle_m$ also increases by ~100 to 1000 K. In the SimA panel of Figure 13, radiative cooling in neutral gas by Lyα and H_2 in SimA-HHe and SimA-RT, respectively, is apparent at the final redshift. In the star formation run, most of the neutral mass fraction lies within the most massive halo and is shielded from radiation from stars within the halo and thus can radiatively cool. This occurs in SimB but to a lesser extent and is not clearly seen in Figure 13.

The effects from radiative feedback are most evident in the average temperatures of ionized gas. The first star in the calculations raises the mass- and volume-averaged temperatures of the ionized gas to 2×10^4 K. Afterward the remnant cools from Compton and adiabatic processes as it expands to temperatures similar to the RT simulations. Photoheating from later stars causes the temperatures in the ionized regions to fluctuate between 3000 and 10,000 K. The supernova calculations are slightly higher due to the hot SN bubble that has an initial temperature of $\sim10^8$ K. The mass-averaged temperature increases more than $\langle T\rangle_v$ because of the photoheating of the host halo and virial heating of the halos, which is the cause of the increase in the simulations without star formation. These increased temperatures cause the photoevaporation and Jeans smoothing of the gas in the relic H II regions. We discuss these effects in the next section.

5. DISCUSSION

We have studied the details of massive metal-free star formation and its role in the start of cosmological reionization. We have treated star formation and radiation in a self-consistent manner, allowing for an accurate investigation of the evolution of cosmic structure under the influence of early Population III stars. Stellar radiation from these stars provides thermal, dynamical,

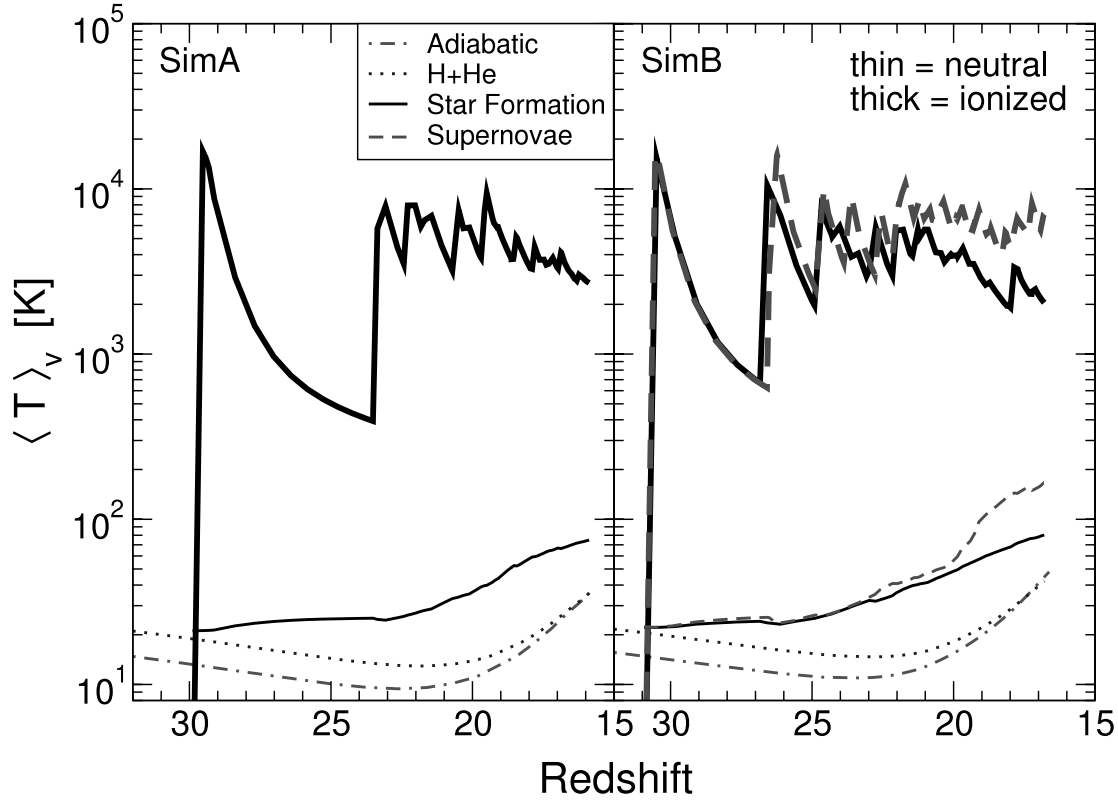

FIG. 12.—Evolution of the volume-averaged temperature in the inner 250 and 300 comoving kpc for SimA (*left*) and SimB (*right*), respectively, for neutral (*thin line*) and ionized (*thick line*; $f_e > 10^{-3}$) gas. The simulations for the adiabatic (*dot-dashed line*), cooling only (*dotted line*), star formation only (*solid line*), and supernovae (*dashed line*) simulations are plotted. [*See the electronic edition of the Journal for a color version of this figure*.]

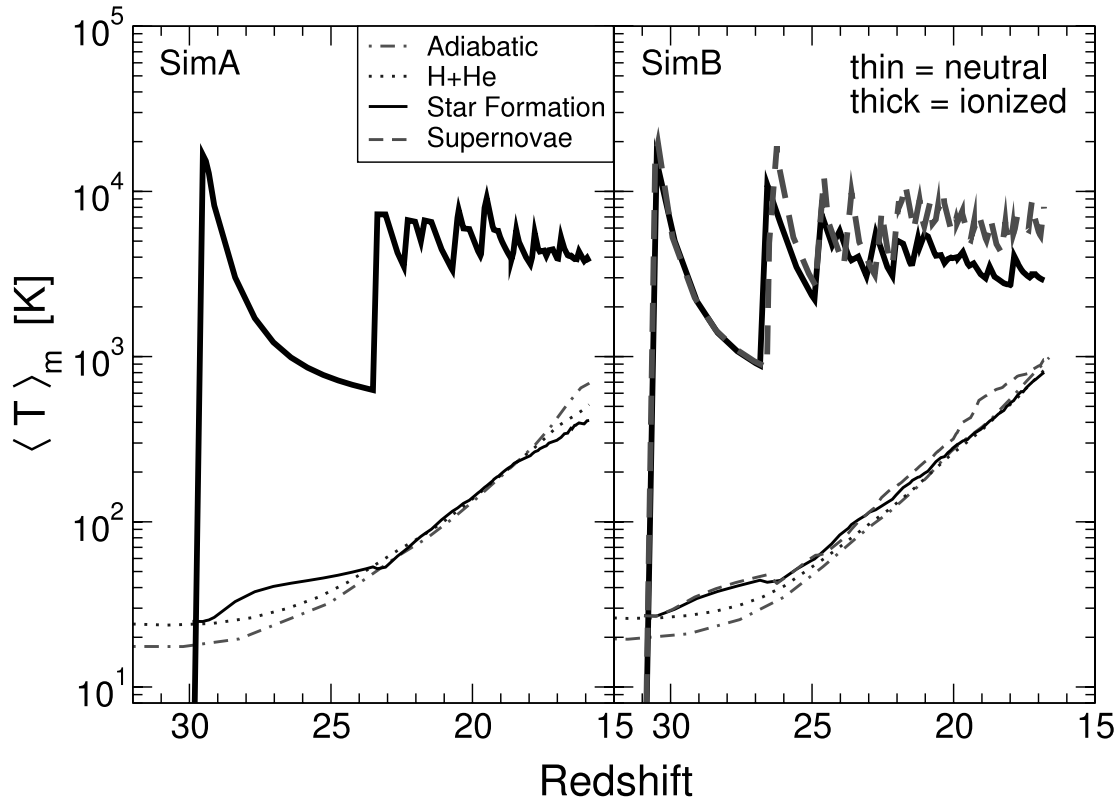

FIG. 13.—Same as Fig. 12, but for the mass-averaged temperature. [*See the electronic edition of the Journal for a color version of this figure*.]

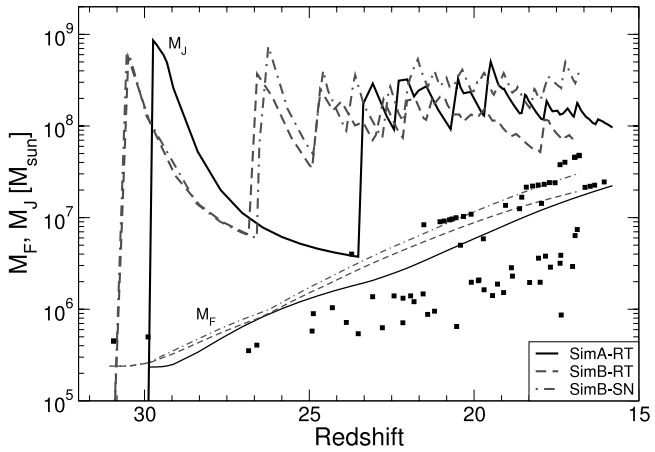

FIG. 14.—Jeans mass M_J and filtering mass M_F that can form bound objects. The squares denote the total mass of star-forming halos in all three simulations. [*See the electronic edition of the Journal for a color version of this figure.*]

and ionizing feedback to the host halos and IGM. Although Population III stars are not thought to provide the majority of ionizing photons needed for cosmological reionization, they play a key role in the early universe because early galaxies that form in these relic H II regions are significantly affected by Population III feedback. Hence it is important to consider primordial stellar feedback while studying early galaxy formation. In this section, we compare our results to previous numerical simulations and semianalytic models of reionization and then discuss any potential caveats of our methods and possible future directions of this line of research.

5.1. *Comparison to Previous Models*

5.1.1. *Filtering Mass*

One source of negative feedback is the suppression of gas accretion into potential wells when the IGM is preheated. The lower limit of the mass of a star-forming halo is the Jeans filtering mass

$$M_F^{2/3}(a) = \frac{3}{a}\int_0^a da' M_J^{2/3}(a')\left[1-\left(\frac{a'}{a}\right)\right], \qquad (12)$$

where a and M_J are the scale factor and time-dependent Jeans mass in the H II region (Gnedin & Hui 1998; Gnedin 2000b). In addition, the virial shocks are weakened if the accreting gas is preheated and will reduce the collisional ionization in halos with $T_{vir} \gtrsim 10^4$ K. To illustrate the effect of Jeans smoothing, we take the large H II region of SimB-SN because it has the largest ionized filling fraction, which is constantly being heated after $z = 21$. Temperatures in this region fluctuate between 1000 and 30,000 K, depending on the proximity of the currently living stars. In Figure 14 we show the resulting filtering mass of regions with an ionization fraction greater than 10^{-3} along with the total mass of star-forming halos.

Gnedin (2000b) found the minimum mass of a star-forming halo is better described by M_F instead of M_J. Our simulations are in excellent agreement for halos that are experiencing star formation after reincorporation of their previously expelled gas. The filtering mass is the appropriate choice for a minimum mass in this case as the halo forms from preheated gas. However, for halos that have already assembled before they become embedded in a relic H II region, the appropriate minimum mass M_{min} is one that is regulated by the LW background (Machacek et al. 2001; Wise & Abel 2005) and photo-evaporation (e.g., Efstathiou 1992; Barkana & Loeb 1999; Haiman et al. 2001; Mesinger et al. 2006). This is evident in the multitude of star-forming halos below M_F. With the exception of star formation induced by SN blast waves or I-fronts, this verifies the justification of using M_{min} and M_F for Population III and galaxy formation, respectively, as a criterion for star-forming halos in semianalytic models.

5.1.2. *Star Formation Efficiency*

Semianalytic models rely on a star formation efficiency $f_\star$, which is the fraction of collapsed gas that forms stars, to calculate quantities such as emissivities, chemical enrichment, and IGM temperatures. Low-mass halos that form a central star have $f_\star \sim 10^{-3}$ whose value originates from a single 100 $M_\odot$ star forming in a dark matter halo of mass $10^6\,M_\odot$ (Abel et al. 2002; Bromm et al. 2002; Yoshida et al. 2006). Population II star-forming halos are usually calibrated with star formation efficiencies from local dwarf and high-redshift starburst galaxies and are usually on the order of a few percent (e.g., Taylor et al. 1999; Gnedin 2000a).

This leads to the question: how efficient is star formation in these high-redshift halos while explicitly considering feedback? This is especially important when halos start to form multiple massive stars and when metallicities are not sufficient to induce Population II star formation. The critical metallicity for a transition to Population II is still unclear. Recently, Jappsen et al. (2007a) showed that metal line cooling is dynamically unimportant in diffuse gas until metallicities of $10^{-2}\,Z_\odot$. On the other hand, dust that is produced in SNe can generate efficient cooling down in dense gas with $10^{-6}\,Z_\odot$ (Schneider et al. 2006). If the progenitors of the more massive halos did not result in a pair-instability SN, massive star formation can continue until it becomes sufficiently enriched. Hence our simulations can probe the efficiency of this scenario of massive metal-free star formation. It has also been suggested that the cosmological conditions that lead to the collapse of a metal-poor molecular cloud ($Z/Z_\odot \approx 10^{-3.5}$) may be more important than some critical metallicity in determining the initial mass function of a given stellar system (Jappsen et al. 2007b).

We calculate $f_\star$ with the ratio of the sum of the stellar masses to the total gas mass of unique star-forming halos. For example at the final redshift of 15.9 in SimA-RT, the most massive halo and its progenitors had hosted 11 stars and the gas mass of this halo is $1.8\times10^6\,M_\odot$, which results in $f_\star = 6.1\times10^{-4}$ for this particular halo. Expanding this quantity to all star-forming halos, $f_\star/10^{-4} =$ 5.6, 6.7, 7.4 for SimA-RT, SimB-RT, and SimB-SN, respectively. We note that our choice of $M_\star = 170\,M_\odot$ in SimB-SN increases $f_\star$ by 70%. Our efficiencies are smaller than the isolated Population III case because halos cannot form any stars once the first star expels the gas, and 40–75 million years must pass until stars can form again when the gas is reincorporated into the halo.

By regarding the feedback created by Population III stars and associated complexities during the assembly of these halos, the $f_\star$ values of $\sim 6\times10^{-4}$ that are explicitly determined from our radiation hydrodynamical simulations provide a more accurate estimate on the early star formation efficiencies.

5.1.3. *Intermittent and Anisotropic Sources*

Our treatment of star formation and feedback produces intermittent star formation, especially in low-mass halos. If one does not account for this, star formation rates might be overestimated in this phase of star formation. Kinetic energy feedback is the main cause of this behavior. As discussed in §§ 3.2 and 4.4, shock waves created by D-type I-fronts and SN explosions expel most of the gas in halos with masses $\lesssim 10^7\,M_\odot$. A period of quiescence follows these instances of star formation. Then stars are able to form after enough material has accreted back into the halo. Only

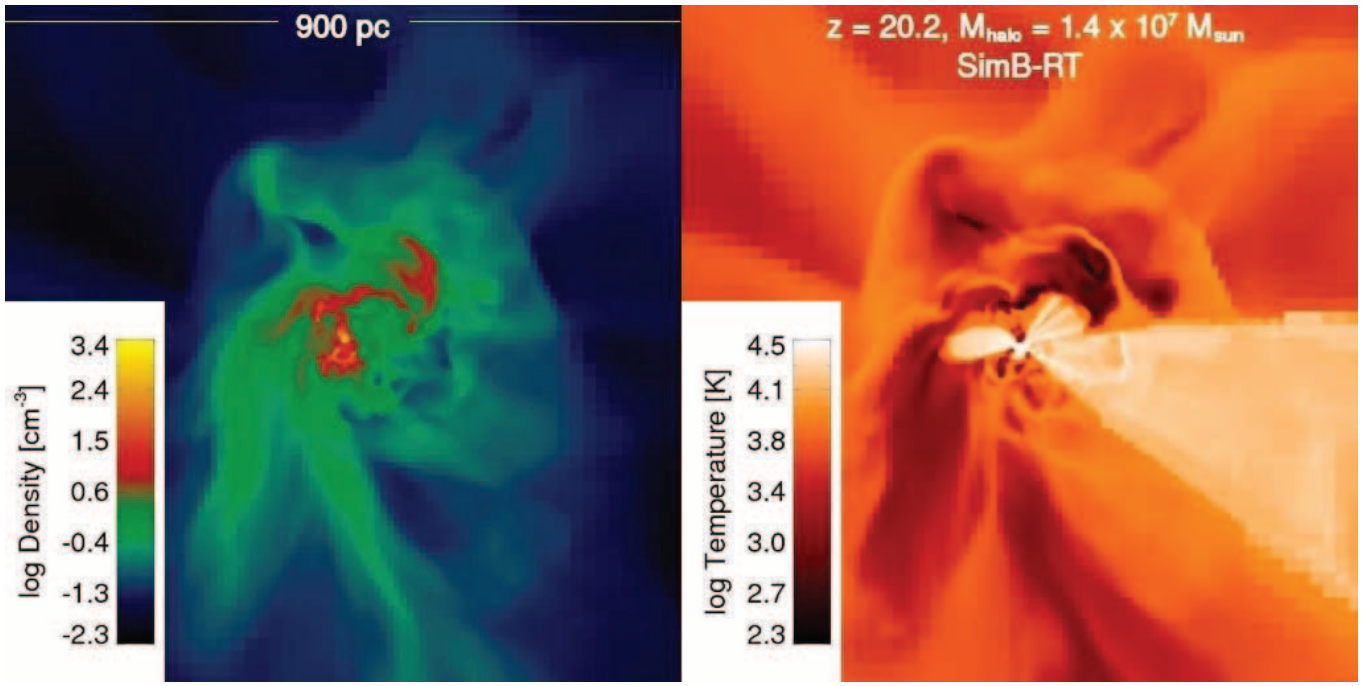

FIG. 15.—Density (*left*) and temperature (*right*) slices of an anisotropic H II region in the most massive halo of SimB-RT. The star has lived for 2.5 Myr out of its 2.7 Myr lifetime. The field of view is 900 proper parsecs.

when the halo becomes massive enough to retain most of the outflows and cool efficiently through Lyα and H_2 radiative processes, star formation becomes more regular with successive stars forming.

The central gas structures in the host halo are usually anisotropic as it is acquiring material through accretion along filaments and mergers. At scales smaller than 10 pc, the most optically thick regions produce shadows where the gas radially behind the dense clump is not photoionized or photoheated by the source. This produces cometary and so-called elephant trunk structures that are also seen in local star-forming regions and have been discussed in detail since Pottasch (1958). At a larger distance, the surrounding cosmic structure is composed of intersecting or adjacent filaments and satellite halos, which breaks spherical symmetry. The filaments and nearby halos are optically thick and remain cool and thus the density structures are largely unchanged. The entropy of dense regions is not increased by stellar radiation and will feel little negative feedback from an entropy floor that only exists in the ionized IGM (see Oh & Haiman 2003). Ray tracing allows for accurate tracking of I-fronts in this inhomogeneous medium. Radiation propagates through the least optically thick path and generates champagne flows that have been studied extensively in the context of present day star formation (e.g., Franco et al. 1990; Churchwell 2002; Shu et al. 2002; Arthur & Hoare 2006). In the context of massive primordial stars, these champagne flows spread into the voids and are impeded by the inflowing filaments. The resulting H II regions have "butterfly" morphologies (Abel et al. 1999, 2007; Alvarez et al. 2006a; Mellema et al. 2006; Yoshida et al. 2007a). We also point out that sources embedded in relic H II largely maintain or increase the ionization fraction. Here the already low optical depth of the recently ionized medium (within a recombination time) allows the radiation to travel to greater distances than a halo embedded in a completely neutral IGM. The H II regions become increasingly anisotropic in higher mass halos. We show an example of the morphology of a H II region near the end of the star's lifetime in a dark matter halo with mass $1.4 \times 10^7\ M_\odot$ in Figure 15.

5.2. *Potential Caveats and Future Directions*

Although we have simulated the first generations of stars with radiation hydrodynamic simulations, our methods have neglected some potentially important processes and made an assumption about the Population III stellar masses.

One clear shortcoming of our simulations is the small volume and limited statistics of the objects studied here. However, it was our intention to focus on the effects of Population III star formation on cosmological reionization and on the formation of an early dwarf galaxy instead of global statistics. The star formation only simulations (SimA-RT and SimB-RT) converge to similar averaged quantities, e.g., ionized fraction, temperatures, star formation rates, at the final redshift. The evolutions of these quantities differ because of the limited number of stars that form in the simulations, which then causes the evolution to depend on individual star formation times. This variance should be expected in the small volumes that we simulate and should not diminish the significance of our results.

We have verified even in a 2.5 σ peak that Population III stars cannot fully reionize the universe, which verified previous conclusions that low-luminosity galaxies provide the majority of ionizing photons. Furthermore, it is beneficial to study Population III stellar feedback because it regulates the nature of star formation in these galaxies that form from preheated material. Further radiation hydrodynamics simulations of primordial star and galaxy formation with larger volumes, while still resolving the first star-forming halos of mass $\sim 3 \times 10^5\ M_\odot$, will improve the statistics of early star formation, especially in more typical overdensities, i.e., 1 σ peaks, some of which could survive to become dwarf spheroidal galaxies at $z = 0$.

In this work we treated the LW radiation field as optically thin, but in reality, H_2 produces a nonzero optical depth above column densities of 10^{14} cm^{-2} (Draine & Bertoldi 1996). Conversely, Doppler shifts of the LW lines arising from large velocity anisotropies and gradient may render H_2 self-shielding unimportant

up to column densities of 10^{20}–10^{21} cm^{-2} (Glover & Brand 2001). If self-shielding is important, it will lead to increased star formation in low-mass halos even when a nearby source is shining. Moreover, H_2 production can also be catalyzed ahead of I-fronts (Ricotti et al. 2001; Ahn & Shapiro 2007). In these halos, LW radiation will be absorbed before it can dissociate the central H_2 core. On the same topic, we neglect any type of soft UV or LW background that is created by sources that are cosmologically nearby ($\Delta z/z \sim 0.1$). A soft UV background either creates positive or negative feedback, depending on its strength (Mesinger et al. 2006), and a LW background increases the minimum halo mass of a star-forming halo (Machacek et al. 2001; Yoshida et al. 2003; O'Shea & Norman 2007; Wise & Abel 2007b). However, in our calculations, the lack of self-shielding, which suppresses star formation in low-mass halos, and the neglect of a LW background, which allows star formation in these halos, may partially cancel each other. Hence one may expect no significant deviations in the SFRs and reionization history if one treats these processes explicitly.

To address the incident radiation and the resulting UV background from more rare density fluctuations outside of our simulation volume, it will be useful to bridge the gap between the start of reionization on Mpc scales to larger scale (10–100 Mpc) simulations of reionization, such as the work of Sokasian et al. (2003), Iliev et al. (2006), Zahn et al. (2007), and Kohler et al. (2007). Radiation characteristics from a volume that has similar overdensities as our Mpc-scale simulations can be sampled from such larger volumes to create a radiation background that inflicts the structures in our Mpc scale simulations. Inversely, perhaps the small-scale evolution of the clumping factor, filtering mass, and average temperature and ionization states can be used to create an accurate subgrid model in large volume reionization simulations.

Another potential caveat is the continued use of primordial gas chemistry in metal-enriched regions in the SN runs. Our simulations with SNe give excellent initial conditions for self-consistently treating the transition to low-mass star formation. In future work we plan to introduce metal-line and dust cooling models (e.g., from Glover & Jappsen 2007; Smith & Sigurdsson 2008) to study this transition.

The one main assumption about Population III stars in our calculations is the fixed, user-defined stellar mass. The initial mass function (IMF) of these stars is largely unknown; therefore, we did not want to introduce an uncertainty by choosing a fiducial IMF. It is possible to calculate a rough estimate of the stellar mass by comparing the accretion rates and Kelvin-Helmholtz time of the contracting molecular cloud (Abel et al. 2002; O'Shea et al. 2005). Protostellar models of primordial stars have also shown that the zero-age main sequence (ZAMS) is reached at 100 $M_\odot$ for typical accretion histories after the star halts its adiabatic contraction (Omukai & Palla 2003; Yoshida et al. 2006). Furthermore, we have neglected HD cooling, which may become important in halos embedded in relic H II regions and result in lower mass ($\sim$30 $M_\odot$) metal-free stars (O'Shea et al. 2005; Greif & Bromm 2006; Yoshida et al. 2007b). Based on accretion histories of star-forming halos, one can estimate the ZAMS stellar mass for each halo and create a more self-consistent and ab initio treatment of Population III star formation and feedback.

6. SUMMARY

We conducted three radiation hydrodynamical, adaptive mesh refinement simulations that supplement our previous cosmological simulations that focused on the hydrodynamics and cooling during early galaxy formation. These new simulations concentrated on the formation and feedback of massive, metal-free stars. We used adaptive ray tracing to accurately track the resulting H II regions and followed the evolution of the photoionized and photoheated IGM. We also explored the details of early star formation in these simulations. Theories of early galaxy formation and reionization and large-scale reionization simulations can benefit from the useful quantities and characteristics of the high-redshift universe, such as SFR and IGM temperatures and ionization states, calculated in our simulations. The key results from this work are listed below.

1. SFRs increase from 5×10^{-4} at redshift 30 to 6×10^{-3} $M_\odot$ yr^{-1} Mpc^{-3} at redshift 20 in our simulations. Afterward the SFR begins to have a bursting nature in halos more massive than 10^7 $M_\odot$ and fluctuates around 10^{-2} $M_\odot$ yr^{-1} Mpc^{-3}. These rates are larger than the ones calculated in Hernquist & Springel (2003) because our simulation volume samples a highly biased region that contains a 2.5 σ density fluctuation. The associated emissivity from these stars increases from 1 to $\sim$100 ionizing photons per baryon per Hubble time between redshifts 15 and 30.

2. In order to provide a comparison to semianalytic models, we calculate the star formation efficiency to be $\sim 6 \times 10^{-4}$ averaged over all redshifts and the simulation volume. For Population III star formation, this is a factor of 2 lower than stars that are not affected by feedback (Abel et al. 2002; Bromm et al. 2002; Yoshida et al. 2006; O'Shea & Norman 2007).

3. Shock waves created by D-type I-fronts expel most of the gas in the host halos below $\sim 5 \times 10^6$ $M_\odot$. Above this mass, significant outflows that are still bound to the halo are generated. This feedback creates a dynamical picture of early structure formation, where star formation is suppressed in halos because of this baryon depletion, which is more effective than UV heating or the radiative dissociation of H_2.

4. We see three instances of induced star formation in halos with masses $\sim 3 \times 10^6$ $M_\odot$. Here a star forms as a SN blast wave overtakes an overdensity created by an ionization front instability. H_2 formation is catalyzed by additional free electrons in the relic H II region and in the SN blast wave (Ferrara 1998).

5. As star formation occurs regularly in the simulation after redshift 25, four (six) ionizing photons are needed per sustained hydrogen ionization. As the most massive halo becomes larger than $\sim 10^7$ $M_\odot$ in the simulations without SNe, H II regions become trapped and ionizing radiation only escapes into the IGM in small solid angles. Hence the number of photons per effective ionization increases to 15 (50). In SimB-SN, stellar radiation from induced star formation has an escape fraction of nearly unity, which occurs four times in the calculation. This allows the IGM to remain ionized at a volume fraction 3 times higher than without SNe. Similarly, the ionizing photon to ionization ratio also stays elevated at 10 : 1 instead of decreasing in the calculations with star formation only.

6. Our simulations that include star formation and H_2 formation capture the entire evolution of the clumping factor that is used in semianalytic models to calculate the effective enhancement of recombinations in the IGM. We showed that clumping factors in the ionized medium fluctuate around 75% of the values found in adiabatic simulations. They evolve from unity at high redshifts and steadily increase to $\sim$4 and 3.5 with and without SNe at $z = 17$, respectively. Photoevaporation from stellar feedback causes the decrease of the clumping factor.

7. We calculated the Jeans filtering mass with the volume-averaged temperature only in fully and partially ionized regions, which yields a better estimate than the temperature averaged over both ionized and neutral regions. The filtering mass depends on the thermal history of the IGM, which mainly cools through

Compton cooling. It increases by 2 orders of magnitude to $\sim 3 \times 10^7\ M_\odot$ at $z \sim 15$. It describes the minimum mass a halo requires to collapse after hosting a Population III star. For halos forming their first star, the minimum halo mass is regulated by the LW background (Machacek et al. 2001) and photoevaporation (e.g., Haiman et al. 2001).

Population III stellar feedback plays a key role in early star formation and the beginning of cosmological reionization. The shallow potential wells of their host halos only amplify their radiative feedback. Our understanding of the formation of the oldest galaxies and the characteristics of isolated dwarf galaxies may benefit from including the earliest stars and their feedback in galaxy formation models. Although these massive stars only partially reionized the universe, their feedback on the IGM and galaxies is crucial to include since it affects the characteristics of low-mass galaxies that are thought to be primarily responsible for cosmological reionization. Harnessing observational clues about reionization, observations of local dwarf spheroidal galaxies, and numerical simulations that accurately handle star formation and feedback may provide great insight on the formation of the first galaxies, their properties, and how they completed cosmological reionization.

The quality and robustness of this paper was improved through the feedback of an anonymous referee. This work was supported by NSF CAREER award AST 02-39709 from the National Science Foundation and partially supported in part by the National Science Foundation under grant PHY05-51164. J. H. W. thanks Renyue Cen for helpful discussions. We benefited from fruitful conversations with Marcelo Alvarez. We are grateful for the continuous support from the computational team at SLAC. We benefited from the hospitality of KITP at UC Santa Barbara, where this work was completed. We performed these calculations on 16 processors of a SGI Altix 3700 Bx2 at KIPAC at Stanford University.

REFERENCES

Abel, T., Anninos, P., Norman, M. L., & Zhang, Y. 1998, ApJ, 508, 518
Abel, T., Anninos, P., Zhang, Y., & Norman, M. L. 1997, NewA, 2, 181
Abel, T., Bryan, G. L., & Norman, M. L. 2000, ApJ, 540, 39
———. 2002, Science, 295, 93
Abel, T., Norman, M. L., & Madau, P. 1999, ApJ, 523, 66
Abel, T., & Wandelt, B. D. 2002, MNRAS, 330, L53
Abel, T., Wise, J. H., & Bryan, G. L. 2007, ApJ, 659, L87
Ahn, K., & Shapiro, P. R. 2007, MNRAS, 375, 881
Alvarez, M. A., Bromm, V., & Shapiro, P. R. 2006a, ApJ, 639, 621
Alvarez, M. A., Shapiro, P. R., Ahn, K., & Iliev, I. T. 2006b, ApJ, 644, L101
Anninos, P., Zhang, Y., Abel, T., & Norman, M. L. 1997, NewA, 2, 209
Arthur, S. J., & Hoare, M. G. 2006, ApJS, 165, 283
Barkana, R., & Loeb, A. 1999, ApJ, 523, 54
Bertschinger, E. 1995, preprint (astro-ph/9506070)
———. 2001, ApJS, 137, 1
Bouwens, R. J., et al. 2004, ApJ, 606, L25
Bowman, J. D., et al. 2007, AJ, 133, 1505
Bromm, V., Coppi, P. S., & Larson, R. B. 2002, ApJ, 564, 23
Bromm, V., & Loeb, A. 2003, ApJ, 596, 34
Bryan, G. L., & Norman, M. L. 1997, in ASP Conf. Ser. 123, Computational Astrophysics, ed. D. A. Clarke & M. Fall (San Francisco: ASP), 363
———. 1999, in Structured Adaptive Mesh Refinement (SAMR) Grid Methods, ed. S. B. Baden, N. P. Chrisochoides, D. Gannon, & M. L. Norman (New York: Springer), 165
Cen, R., & Ostriker, J. P. 1992, ApJ, 399, L113
Churchwell, E. 2002, ARA&A, 40, 27
Cooray, A., et al. 2007, ApJ, 659, L91
Crocce, M., Pueblas, S., & Scoccimarro, R. 2006, MNRAS, 373, 369
Dekel, A., & Silk, J. 1986, ApJ, 303, 39
Draine, B. T., & Bertoldi, F. 1996, ApJ, 468, 269
Efstathiou, G. 1992, MNRAS, 256, 43P
Eisenstein, D. J., & Hut, P. 1998, ApJ, 498, 137
Eyles, L. P., Bunker, A. J., Ellis, R. S., Lacy, M., Stanway, E. R., Stark, D. P., & Chiu, K. 2007, MNRAS, 374, 910
Fan, X., et al. 2006, AJ, 132, 117
Ferrara, A. 1998, ApJ, 499, L17
Franco, J., Tenorio-Tagle, G., & Bodenheimer, P. 1990, ApJ, 349, 126
Gardner, J. P., et al. 2006, Space Sci. Rev., 123, 485
Gehrels, N., et al. 2004, ApJ, 611, 1005
Glover, S. C. O., & Brand, P. W. J. L. 2001, MNRAS, 321, 385
Glover, S. C. O., & Jappsen, A.-K. 2007, ApJ, 666, 1
Gnedin, N. Y. 2000a, ApJ, 535, L75
———. 2000b, ApJ, 542, 535
Gnedin, N. Y., & Hui, L. 1998, MNRAS, 296, 44
Greif, T. H., & Bromm, V. 2006, MNRAS, 373, 128
Haehnelt, M. G. 1995, MNRAS, 273, 249
Haiman, Z., Abel, T., & Madau, P. 2001, ApJ, 551, 599
Haiman, Z., Thoul, A. A., & Loeb, A. 1996, ApJ, 464, 523
Heger, A., & Woosley, S. E. 2002, ApJ, 567, 532
Hernquist, L., & Springel, V. 2003, MNRAS, 341, 1253
Hui, L., & Haiman, Z. 2003, ApJ, 596, 9
Iliev, I. T., Mellema, G., Pen, U.-L., Merz, H., Shapiro, P. R., & Alvarez, M. A. 2006, MNRAS, 369, 1625
Iliev, I. T., Shapiro, P. R., & Raga, A. C. 2005, MNRAS, 361, 405
Jappsen, A.-K., Glover, S. C. O., Klessen, R. S., & Mac Low, M.-M. 2007a, ApJ, 660, 1332
Jappsen, A.-K., Klessen, R. S., Glover, S. C. O., & Mac Low, M.-M. 2007b, ApJ, submitted (arXiv:0709.3530)
Johnson, J. L., Greif, T. H., & Bromm, V. 2007, ApJ, 665, 85
Kashlinsky, A., Arendt, R. G., Mather, J., & Moseley, S. H. 2007, ApJ, 654, L1
Kitayama, T., & Yoshida, N. 2005, ApJ, 630, 675
Kitayama, T., Yoshida, N., Susa, H., & Umemura, M. 2004, ApJ, 613, 631
Kohler, K., Gnedin, N. Y., & Hamilton, A. J. S. 2007, ApJ, 657, 15
Lukić, Z., Heitmann, K., Habib, S., Bashinsky, S., & Ricker, P. M. 2007, ApJ, 671, 1160
Machacek, M. E., Bryan, G. L., & Abel, T. 2001, ApJ, 548, 509
Madau, P., Ferguson, H. C., Dickinson, M. E., Giavalisco, M., Steidel, C. C., & Fruchter, A. 1996, MNRAS, 283, 1388
Mellema, G., Iliev, I. T., Alvarez, M. A., & Shapiro, P. R. 2006, NewA, 11, 374
Mesinger, A., Bryan, G. L., & Haiman, Z. 2006, ApJ, 648, 835
Nagakura, T., & Omukai, K. 2005, MNRAS, 364, 1378
Oh, S. P., & Haiman, Z. 2003, MNRAS, 346, 456
Omukai, K., & Palla, F. 2003, ApJ, 589, 677
Onken, C. A., & Miralda-Escudé, J. 2004, ApJ, 610, 1
O'Shea, B. W., Abel, T., Whalen, D., & Norman, M. L. 2005, ApJ, 628, L5
O'Shea, B. W., & Norman, M. L. 2007, ApJ, 654, 66
Page, L., et al. 2007, ApJS, 170, 335
Pottasch, S. R. 1958, Rev. Mod. Phys., 30, 1053
Press, W. H., & Schechter, P. 1974, ApJ, 187, 425
Reed, D. S., Bower, R., Frenk, C. S., Jenkins, A., & Theuns, T. 2007, MNRAS, 374, 2
Ricotti, M., Gnedin, N. Y., & Shull, J. M. 2001, ApJ, 560, 580
———. 2002a, ApJ, 575, 33
———. 2002b, ApJ, 575, 49
Rottgering, H. J. A., et al. 2006, preprint (astro-ph/0610596)
Schaerer, D. 2002, A&A, 382, 28
Schaye, J., Theuns, T., Rauch, M., Efstathiou, G., & Sargent, W. L. W. 2000, MNRAS, 318, 817
Schilizzi, R. T. 2004, Proc. SPIE, 5489, 62
Schneider, R., Omukai, K., Inoue, A. K., & Ferrara, A. 2006, MNRAS, 369, 1437
Scoccimarro, R. 1998, MNRAS, 299, 1097
Shapiro, P. R. 1986, PASP, 98, 1014
Shapiro, P. R., Iliev, I. T., & Raga, A. C. 2004, MNRAS, 348, 753
Shapiro, P. R., Raga, A. C., & Mellema, G. 1997, Proc. 13th IAP Astrophysics Colloquium, Structure and Evolution of the Intergalactic Medium from QSO Absorption Line Systems, ed. P. Petitjean & S. Charlot (Paris: Editions Frontières), 41
Sheth, R. K., & Tormen, G. 2002, MNRAS, 329, 61
Shu, F. H. 1992, Physics of Astrophysics, Vol. 2 (Sausalito: University Science Books)
Shu, F. H., Lizano, S., Galli, D., Cantó, J., & Laughlin, G. 2002, ApJ, 580, 969
Smith, B. D., Sigurdsson, S., & Abel, T. 2008, MNRAS, 385, 1443
Sokasian, A., Abel, T., Hernquist, L., & Springel, V. 2003, MNRAS, 344, 607
Spergel, D. N., et al. 2003, ApJS, 148, 175
———. 2007, ApJS, 170, 377

Swarup, G., Ananthakrishnan, S., Kapahi, V. K., Rao, A. P., Subrahmanya, C. R., & Kulkarni, V. K. 1991, Curr. Sci., 60, 95
Taylor, C. L., Hüttemeister, S., Klein, U., & Greve, A. 1999, A&A, 349, 424
Tegmark, M., Silk, J., Rees, M. J., Blanchard, A., Abel, T., & Palla, F. 1997, ApJ, 474, 1
Thompson, R. I., Eisenstein, D., Fan, X., Rieke, M., & Kennicutt, R. C. 2007, ApJ, 666, 658
Whalen, D., Abel, T., & Norman, M. L. 2004, ApJ, 610, 14
———. 2008a, ApJ, 672, 287
———. 2008b, ApJ, 673, 664
Whalen, D., O'Shea, B. W., Smidt, J., & Norman, M. L. 2008, ApJ, 679, 925
Wilson, T. L., Beasley, A. J., & Wootten, H. A. 2005, in ASP Conf. Ser. 344, The Cool Universe: Observing Cosmic Dawn, ed. N. E. Kassim, M. R. Pérez, W. Junor, & P. A. Henning (San Francisco: ASP), 232
Wise, J. H., & Abel, T. 2005, ApJ, 629, 615
———. 2007a, ApJ, 665, 899
———. 2007b, ApJ, 671, 1559
———. 2007c, ApJ, submitted (arXiv: 0710.3160)
Yoshida, N., Abel, T., Hernquist, L., & Sugiyama, N. 2003, ApJ, 592, 645
Yoshida, N., Oh, S. P., Kitayama, T., & Hernquist, L. 2007a, ApJ, 663, 687
Yoshida, N., Omukai, K., & Hernquist, L. 2007b, ApJ, 667, L117
Yoshida, N., Omukai, K., Hernquist, L., & Abel, T. 2006, ApJ, 652, 6
Zahn, O., Lidz, A., McQuinn, M., Dutta, S., Hernquist, L., Zaldarriaga, M., & Furlanetto, S. R. 2007, ApJ, 654, 12
Zaldarriaga, M., Hui, L., & Tegmark, M. 2001, ApJ, 557, 519